# Weakly Supervised Object Segmentation by Background Conditional Divergence

**Anonymous authors**
**Paper under double-blind review**

## Abstract

As a computer vision task, automatic object segmentation remains challenging in specialized image domains without massive labeled data, such as synthetic aperture sonar images, remote sensing, biomedical imaging, etc. In any domain, obtaining pixel-wise segmentation masks is expensive. In this work, we propose a method for training a masking network to perform binary object segmentation using weak supervision in the form of image-wise presence or absence of an object of interest, which provides less information but may be obtained more quickly from manual or automatic labeling. A key step in our method is that the segmented objects can be placed into background-only images to create realistic, images of the objects with counterfactual backgrounds. To create a contrast between the original and counterfactual background images, we propose to first cluster the background-only images, and then during learning create counterfactual images that blend objects segmented from their original source backgrounds to backgrounds chosen from a targeted cluster. One term in the training loss is the divergence between these counterfactual images and the real object images with backgrounds of the target cluster. The other term is a supervised loss for background-only images. While an adversarial critic could provide the divergence, we use sample-based divergences. We conduct experiments on side-scan and synthetic aperture sonar in which our approach succeeds compared to previous unsupervised segmentation baselines that were only tested on natural images. Furthermore, to show generality we extend our experiments to natural images, obtaining reasonable performance with our method that avoids pretrained networks, generative networks, and adversarial critics.

## 1 Introduction

Automatic foreground object segmentation is a computer vision task with a variety of applications in many fields such as medicine, autonomous driving, and defense (Ma et al., 2024; Song et al., 2024; Lee et al., 2024; Cao et al., 2024; Gao et al., 2024; Marinov et al., 2024; Kamtam et al., 2025). Supervised machine learning approaches are limited by the availability of supervised training annotations, such as object masks or bounding boxes, which in specialized domains are expensive to obtain (Russakovsky et al., 2015; Bakas et al., 2017; Sohn et al., 2020). Weak supervision in the form of image-level labels is often sufficient to guide segmentation. In particular, a well-trained classifier can provide class-activation maps to guide segmentation (Kumar Singh & Jae Lee, 2017; Wei et al., 2017; Zhang et al., 2018; Li et al., 2018; Xu et al., 2022; Xie et al., 2022). Prior work on unsupervised learning for object segmentation build off either pretrained classifiers, or the underlying feature extraction backbone networks (Remez et al., 2018; Li et al., 2023; Dosovitskiy et al., 2021; Hamilton et al., 2022; Zhang et al., 2018; Xie et al., 2022). However, for specialized imaging domains, such as sonar and medical images, there are not large crowd-sourced labeled datasets, and the limited datasets that *are* available differ in sensors and contexts that make it difficult to pretrain useful models. Thus, we consider the weakly supervised task for which no pretrained networks are available, where the dataset consists of two sets of images: one labeled as having an object (i.e., composite images) and the other as having no object (i.e., background-only images), which can be obtained through a combination of expert annotation, supervised image-level classification, and human-in-the-loop active learning.

Our goal is to train a neural network to generate binary pixel-wise segmentation masks that separate salient foreground objects from the background. A motivating possibility for such a network is the ability to generate synthetic images composed of an object extracted from one image and background pixels from another.image (Ostyakov et al., 2018). This synthetic image, created by alpha-blending a composite image and a background-only image, is referred to as a counterfactual image, as the background is counterfactual to the original background. While the automatic creation of counterfactual images is independently useful for augmenting training datasets to resolve spurious correlations between objects and their background, these counterfactual images are key to our approach as the network is trained to minimize the statistical divergence between the distributions of real images and the counterfactual images.[1] To minimize this loss, the learned masks must generate counterfactual images that are statistically similar to the real images. However, without further specification this loss is minimized by a degenerate masking that segments the entire image as the object such that after alpha-blending the output is the original input images. Other work on unsupervised segmentation, which lacks the additional set of background-only images, has used the generators and discriminators underlying generative adversarial networks (GANs) along with additional loss terms to avoid such degenerate solutions (Bielski & Favaro, 2019; Sauer & Geiger, 2021; Zou et al., 2023; Yang et al., 2022b). Another solution proposed by Ostyakov et al. (2018) is to use a generative network to inpaint missing portions of the background after applying the complement mask, which should then be background only, and then calculate the divergence between inpainted images and real background-images.

In contrast, our novel approach to avoid the degenerate solution is relatively straightforward: firstly, we organize all images into clusters based on their background content; secondly, we form counterfactuals with background-only images taken from a target cluster that differs from original background cluster; and finally, we compute the conditional divergence between these counterfactual and real images. Although there are multiple ways to achieve background clustering, we choose to perform K-means clustering (or a modified version that seeks balanced clusters) in a latent space obtained from training either an autoencoder (AE) with reconstruction loss or an encoder with self-supervised contrastive learning on the background-only images. For datasets where foreground objects are roughly centered, the background content can be inferred from random crops near edges and corners. In cases where composite images with objects are patches taken from a larger image, the background is inferred from nearby patches without objects. The approach is summarized in Figure 1. Using the average of the conditional divergences across all clusters as a loss encourages the masking network to learn meaningful segmentations by leveraging background variations while effectively isolating foreground objects.

The differences between our approach and the majority of the other work reviewed in Section 2 can be summarized in the following:

1. We assume access to two types of images: composite images (i.e., images that contain foreground objects on a background) and background-only images. *These are the only labels that we assume to be available.*
2. The model consists of a masking network whose output is used to alpha-blend the input composite image with a background-only images, producing a synthetic, counterfactual image.
3. During training, we compute the conditional statistical divergence between background-conditioned counterfactual images and real composite images, and we compute a supervised cost for background-only images.
4. Our approach is relatively straightforward; it consists of a single masking network with a composite loss that is a sum of the two terms, without extensive hyperparameters.
5. We do not rely on pretrained models, affording our research the benefit of achieving satisfactory object segmentation results even with limited datasets of modalities, for which pretrained models are unavailable.

[1] We assume the object can be placed on an independently chosen background. This assumption is valid in underwater sonar where a man-made object's location is largely independent of the background. However, in natural imagery there is much stronger dependence between the object and location within the image, due to depth and context, a problem addressed in other work (Zhu et al., 2023).

In particular, Table 4 shows that the related work suffer from at least one undesired attribute of requiring: pretrained models, adversarial training which is known for its instability, labeled data (e.g., class information), or extensive hyperparameter search for a complicated loss function combination (i.e., not minimalist).

We evaluate the effectiveness of our segmentation approach on the following datasets:

1. **Toy datasets** created by combining canonical datasets (e.g., MNIST, Fashion MNIST (Xiao et al., 2017), and dSprites (Matthey et al., 2017)) with textured backgrounds (Brodatz, 1966). We show that existing unsupervised segmentation benchmarks (Bielski & Favaro, 2019; Xie et al., 2022) fail to converge to an acceptable segmentation on these datasets.

2. **Side-Scan Sonar (SSS) images** containing various foreground objects such as shipwrecks and rocks (Sethuraman et al., 2024). We show that our methodology provides finer-grained details for foreground objects compared to the available ground truth.

3. **Synthetic Aperture Sonar (SAS) images** (Cobb & Zare, 2014), where artificial objects are pasted onto real sonar backgrounds.

4. **Natural images from the CUB-200-2011 dataset** (Wah et al., 2011), which consists of bird images without background-only samples. Our approach performs reasonably well on this dataset, achieving an average precision of up to 50%.

## 2 Related Work

Our weakly supervised foreground object segmentation is most closely related to prior work on unsupervised foreground object segmentation (Bielski & Favaro, 2019; Sauer & Geiger, 2021; Zou et al., 2023; Yang et al., 2022b). These methods either depend on adversarial training (Ostyakov et al., 2018; Remez et al., 2018; Bielski & Favaro, 2019; Chen & Konukoglu, 2018; Singh et al., 2019; He et al., 2022; Yang et al., 2022a; Zou et al., 2023; Sauer & Geiger, 2021; Li et al., 2023), make assumptions about the foreground object size (Bielski & Favaro, 2019; He et al., 2022; Yang et al., 2022b; Zou et al., 2023; Sauer & Geiger, 2021), depend on a given initial mask (Li et al., 2023), need an extensive hyperparameters search (Li et al., 2018; Remez et al., 2018; Bielski & Favaro, 2019; Singh et al., 2019; He et al., 2022; Yang et al., 2022b; Zou et al., 2023; Sauer & Geiger, 2021; Hung et al., 2019; Savarese et al., 2021), depend on pre-trained models or foreground labels (e.g., birds classes) (Remez et al., 2018; Sauer & Geiger, 2021; Li et al., 2023; Dosovitskiy et al., 2021; Hamilton et al., 2022; Wang et al., 2023b; Zhang et al., 2018; Li et al., 2018; Hou et al., 2018; Jiang et al., 2019; Chang et al., 2020; Lee et al., 2021; Wu et al., 2021; Xie et al., 2022; Hung et al., 2019), require stochastic generation or complicated combinations of losses to avoid degenerate solutions (Ostyakov et al., 2018; Li et al., 2018; Remez et al., 2018; Bielski & Favaro, 2019; Hung et al., 2019; Zou et al., 2023; Yang et al., 2022b). Our proposed method, on the other hand, does not depend on any of that. The difference is that we assume access to background-only images that follow the same distribution of backgrounds in the composite images. (Ostyakov et al. (2018) also use this assumption but have adversarial discriminator along with an enhancement and inpainting network.) While purely unsupervised learning without any background-only images is even more challenging, in practice background-only images can be obtained from the surrounding of images with an object, and are naturally obtained through the weak labeling process.

Furthermore, the majority of related work has focused on natural images, where there is often visible differences between objects and background due to the optics. Additionally, in other imaging domains, there may also be a lack of pretrained models. In the case of underwater sonar imagery, which is a specialized and limited domain, even more so than standardized medical imaging (Ma et al., 2024), with datasets limited by the diversity of objects and sensors (Valdenegro-Toro et al., 2021; Preciado-Grijalva et al., 2022). Nonetheless, self-supervised pretraining before classification is possible (Preciado-Grijalva et al., 2022). We found that the majority of the work on unsupervised segmentation of sonar imagery is concerned with sea floor segmentation (Sun et al., 2022; Abu & Diamant, 2017; Yao et al., 2000) or object detection (Abu & Diamant, 2018; Wei et al., 2024). One recent work did investigate generating new sonar imagery using a mask-conditioned diffusion model (i.e., counterfactual images); however they did not explicitly address segmentation (Yang et al., 2024).

A description of related work is included in Appendix A, and summarized in Table 4, which notes which works depend on pretrained models, GAN training, or data labels (e.g., foreground labels). The table highlights that prior work has at least one of these undesirable criteria, which makes it hard to be applied to data-scarce domains such as sonar images.

## 3 Methodology

Our methodology trains a masking network by using its output to alpha-blend the input composite image with an independent background-only image creating a counterfactual image. The training loss consists of two terms; the first is a measure of the statistical divergence between counterfactual and real composite images, and the second is a pixel-wise supervised loss that encourages the alpha-blended output to match the input for background-only images. To avoid degenerate solutions we rely on conditioning the divergence based on different background clusters, which we derive from an auto-encoder or contrastive-learning based representation. Additionally, we consider an extra loss for the masks of composite images that forces a portion of the mask to not be background, which is applicable if the object size is known a priori. Our approach requires minimal hyper-parameter tuning, namely the number of clusters, epochs, and batch size. For architectures we use a U-Net (Ronneberger et al., 2015b), which is a standard neural network architecture, as the masking network and minimal auto-encoder or encoder-only architectures for the latent representation of backgrounds. Figure 1 summarizes the approach.

### 3.1 Problem Formulation

We assume two distributions of images: composite images that contain objects surrounded by background and background-only images that do not have salient objects. Let $\mathcal{I} \subset \mathbb{R}^{m \times n \times c}$ denote the space of images with $c$ channels and $m \times n$ pixels, $\mathcal{X} \subset \mathcal{I}$ denote the space of composite images, and $\mathcal{R} \subset \mathcal{I}$ denote the space of background images. Similar to the generative assumptions in the layered GAN (Bielski & Favaro, 2019; Yang et al., 2022b; Zou et al., 2023), we assume a composite image $X_R \in \mathcal{X}$ generated according to

$$X_R = M \circ F + (\mathbf{1} - M) \circ R, \tag{1}$$

where $R \in \mathcal{R}$ is a background-only image, $F \in \mathcal{I}$ is an image of an object paired with a binary mask $M \in \{0,1\}^{m \times n}$ ($M_{ij} = 1$ if the pixel is object and $M_{ij} = 0$ if the pixel is background), and $\mathbf{1}$ is a $m \times n \times c$-array of ones. The unsupervised segmentation goal is to learn to infer $M$ given only $X_R$.

Probabilistically, as a random variable $X_R \sim \mathbb{P}_X$ is a function of the dependent random variables $(F, M, R) \sim \mathbb{P}_{M,F,R}$, since the object and the background are dependent. However, we assume $R \sim \mathbb{P}_R$ is independent of $(F, M) \sim \mathbb{P}_{M,F}$. Under this assumption, one can generate

$$X_{R'} = M \circ X_R + (\mathbf{1} - M) \circ R', \tag{2}$$

which is an image with the same object (and mask), but a different background $R' \sim \mathbb{P}_R$. While $X_R$ and $R'$ represent real images, $X_{R'}$ is a counterfactual that is a function of $M$. If the independence assumptions hold, $X_{R'} \sim \mathbb{P}_X$.

A masking network is a function $M_\theta : \mathcal{I} \to [0,1]^{m \times n}$, parameterized by $\theta$, that models the relationship between $X_R$ and $M$. Unlike, supervised segmentation the latter is never observed. An ideal masking network would yield the true mask $M_{\theta^*}(X_R) = M$ when applied to a composite image, and would yield an all-zeros mask $\mathbf{0}$ when applied to a background only image $M_{\theta^*}(R) = \mathbf{0}$. The output mask is used to alpha-blend a composite image with an independent background-only image $R'$,

$$\tilde{X}_{R'} = M_\theta(X_R) \circ X_R + (\mathbf{1} - M_\theta(X_R)) \circ R' \in \tilde{\mathcal{X}} \subset \mathcal{I} \tag{3}$$

The goal is then to make the distribution of $\tilde{X}_{R'}$, $\mathbb{P}_{\tilde{X}}$ statistically indistinguishable from $\mathbb{P}_X$. However, directly minimizing a statistical divergence between $\mathbb{P}_{\tilde{X}}$ and $\mathbb{P}_X$ leads to a trivial solution where the masking network always produces a mask of all ones (all foreground),

$$M_{\text{degen}} : X \mapsto \mathbf{1} = \arg\min_{M_\theta} D(\mathbb{P}_{\tilde{X}}, \mathbb{P}_X), \tag{4}$$

since $\tilde{X}_{R'} = M_{\text{degen}}(X_R) \circ X_R + (\mathbf{1} - M_{\text{degen}}(X_R)) \circ R' = X_R \sim \mathbb{P}_X$, a problem also encountered and addressed in different ways in GAN-based approaches for unsupervised segmentation (Bielski & Favaro, 2019; Yang et al., 2022b; Zou et al., 2023) and weakly supervised segmentation (Ostyakov et al., 2018).

To overcome this without the use of GANs, we create a distributional shift between $R$ and $R'$ based on the background portion of the composite image $X_R$ and the background-only image $R'$. The intuition is that restricting the counterfactuals to be generated from source backgrounds that are different than the backgrounds of the target composite images background, discourages masks from retaining any dissimilar background as that would increase the divergence. Specifically, we assume $(R, C_b) \sim \mathbb{P}_{R,C_b}$ is a joint distribution over background images and a latent background class $C_b \in \{1, \ldots, K\}$. The latent variable $C_b$ carries information about the background. Let $\mathbb{P}_{X|C_b=c}$ represent the distribution of composite images generated under the condition that the background image belongs to class $c \in \{1, \ldots, K\}$. When computing the divergence the goal is to target composite images with a specific background class $\mathbb{P}_{X|C_b=c}$, generating counterfactuals from independent background-only images of the same class $R_c \sim \mathbb{P}_{R|C_b=c}$ and sourcing composite images that do not have this class $X_{\neg c} = X_{R|C_b \neq c} \sim \mathbb{P}_{X|C_b \neq c}$, where $\mathbb{P}_{R|C_b \neq c}$ is the distribution over other background classes, such that $X_c \sim \mathbb{P}_{X|C_b=c}$ and $X_{\neg c}$ are independent random variables with different distributions. The masking network's counterfactual image with background from class $c$ is

$$\tilde{X}_c = M_\theta(X_{\neg c}) \circ X_{\neg c} + (1 - M_\theta(X_{\neg c})) \circ R_c \sim \mathbb{P}_{\tilde{X}_{c,\theta}}. \tag{5}$$

Figure 1 shows a diagram of the counterfactual background-conditional image generation process.

The goal is to optimize the parameters $\theta$ of the masking network $M_\theta$ in terms of a the background conditional divergence between the distributions of $\mathbb{P}_{X|C_b=c}$ and $\mathbb{P}_{\tilde{X}_{c,\theta}}$,

$$\mathcal{L}_D(\theta) = \sum_c D(\mathbb{P}_{\tilde{X}_{c,\theta}},\ \mathbb{P}_{X|C_b=c}). \tag{6}$$

Due to the distinct distribution of $X_{\neg c}$ and $X_c$, the trivial masking solution will not minimize the divergence between $\mathbb{P}_{\tilde{X}_{c,\theta}}$ and $\mathbb{P}_{X|C_b=c}$, $M_{\text{degen}}(X_{\neg c}) \circ X_{\neg c} + (\mathbf{1} - M_{\text{degen}}(X_{\neg c})) \circ R_c = X_{\neg c}$ is clearly not distributed according to $\mathbb{P}_{X|C_b=c}$.

Since we assume a sample of background-only images, we also train the masking network to determine if there is an object in the input image (by outputting an all zero mask). While a binary cross-entropy loss could be used per pixel, we use the squared error loss

$$\mathcal{L}_{Bg}(\theta) = \mathbb{E}_R \left[ \sum_{ij} [M_\theta(R)]_{ij}^2 \right] = \mathbb{E}_R \left[ \|M_\theta(R)\|_F^2 \right]. \tag{7}$$

The optimization problem for training the masking network is then

$$\min_{\theta \in \Theta} \mathcal{L}_D(\theta) + \mathcal{L}_{Bg}(\theta), \tag{8}$$

where $\Theta$ is the set of possible parameters for the masking network.

### 3.2 Statistical Divergence Choice

The choice of the divergence $D$ will necessarily impact performance, computational cost, and the learning dynamics. To connect our approach to supervised segmentation tasks, the Wasserstein-2 distance is natural as it seeks a joint distribution $\mathbb{P}_{\tilde{X}_c X_c}$ that pairs the counterfactual $\tilde{X}_c$ and composite image $X_c$ to be as close as possible in a root-mean squared error sense

$$\mathrm{W}_2(\mathbb{P}_{\tilde{X}_{c,\theta}}, \mathbb{P}_{X|C_b=c}) = \inf_{\mathbb{P}_{\tilde{X}_c X_c} \in \mathcal{P}} \sqrt{\mathbb{E}_{(\tilde{X}_c, X_c) \sim \mathbb{P}_{\tilde{X}_c X_c}} \|\tilde{X}_c - X_c\|_2^2}, \tag{9}$$

where $\mathcal{P}$ is the set of joint distributions with marginals equal to $\mathbb{P}_{\tilde{X}_{c,\theta}}$ and $\mathbb{P}_{X|C_b=c}$. The ideal joint distribution would pair the object in $X_c$ with a corresponding object in $\tilde{X}_{\neg c}$ and the background of $X_c$ with a

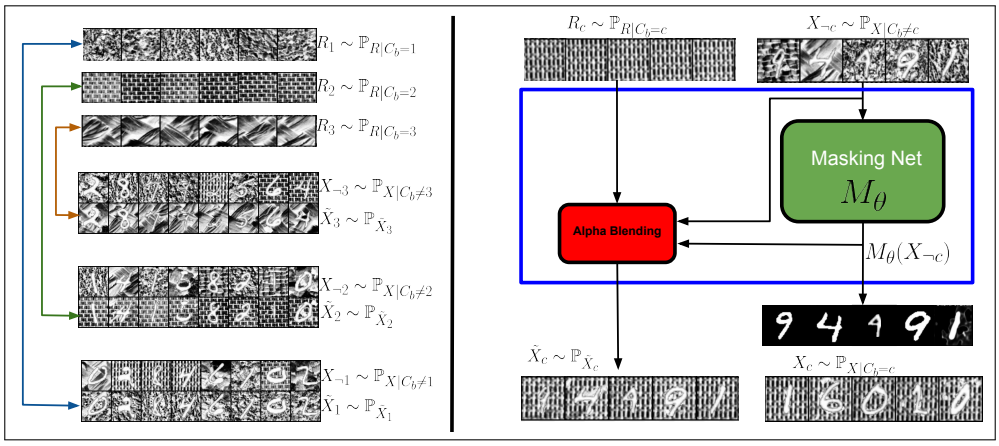


Figure 1: Right: The counterfactual generation model employs a masking network, $M_\theta$, to process composite images, $(X_{\neg c})$, which contain backgrounds other than $c$. These composite images are combined with corresponding background images, $R_c$, of background $c$. The model generates a mask to separate the object from the background, and alpha-blending (as per equation 1) is used to combine the composite images and background images. This results in a counterfactual image that retains the foreground object from $X_{\neg c}$ but places it against a different background. In this instance, the counterfactual image preserves the foreground object in $X_{\neg c}$ but is presented against a distinct background. Left: Demonstration of the inputs and the outputs of the proposed framework indicated by the blue box on the right. The first three rows display different sets of background images, where each set belongs to the same background label. Each subsequent pair of rows shows composite images with various backgrounds, excluding the target background (indicated by the two headed arrow). The second row in each pair presents the generated counterfactual images, where the foreground object is pasted onto the target background using the model on the right.

corresponding background $R_c$ such that $\tilde{X}_c$ would match $X_c$ if the masking is correct. However, if the masking network is wrong the optimal joint distribution may create non-ideal pairings to compensate, possibly leading to local minima. Furthermore, estimating the Wasserstein distance in this primal form is challenging. Based on a review of divergences, including alternatives for the Wasserstein distance, in Appendix B, we select $D$ to be the energy-based sliced Wasserstein (EBSW) distance (Nguyen & Ho, 2023), which avoids adversarial training of discriminators required for the variational estimates of $f$-divergences in GANs (Goodfellow et al., 2014; Nowozin et al., 2016) and has desirable computational and statistical characteristics—in particular it does not suffer from curse of dimensionality (Nguyen & Ho, 2023)—making it broadly applicable without many hyper-parameters. For the hyper-parameters of the estimate of the EBSW, described by equation 14 in Appendix B, we choose $p = 2$ to match equation 9, $f$ to be the exponential function, and $L = 1000$ slices.

### 3.3 Background Clustering

Generally, we do not assume access to the background class/cluster, although in certain situations this side information is known. We propose to use data-driven clustering to assign a cluster label as surrogate for $C_b$ for each image (both composite and background-only images). While directly inferring a background cluster for an image containing an object that takes up the majority of the image may be difficult, in many cases access to wider crops containing mostly background may be possible, which is the case with sonar imagery.

For clustering the backgrounds, we propose using a two-stage process of either an autoencoder (AE) or an encoder trained with self-supervised contrastive learning (CL) followed by K-means on the encoders output. The positive pair in the CL setting is defined as a randomly cropped background image (no less than 80%) and resized to match the original image.

Instead of K-means, we also implement an optimal transport K-means to encourage the cluster distribution to be uniform. That is for each K-means iteration, we run the Sinkhorn algorithm (Cuturi, 2013), using the

Euclidean cost matrix between input data points and the centroids, with a uniform distribution for both, to yield a transportation plan that is cluster balanced. Due to the entropic regularization intrinsic to the Sinkhorn algorithm, each input point is distributed to multiple centroids. Before updating the centroids, new hard assignments are obtained from the highest mass in each row.

The encoder training and subsequent cluster assignment can be applied to all or a subset of the background-only images. Then, during the training of the masking network background-only images and composite images (or mostly background images from nearby crops) are assigned based on the nearest cluster to their encoding, yielding the label $C_b$.

### 3.4 Data

While our goal is to perform real-world weakly supervised object segmentation on sonar images, datasets with ground truth labels are limited. We developed and initially validated our proposed method on artificial single-channel data constructed from combining real-world backgrounds—either textures (photographic images of materials with various textures (Brodatz, 1966) under controlled lighting) or seafloor images obtained from sonar (Cobb & Zare, 2014)—with objects from standard object classification datasets: standard MNIST, FashionMNIST (Xiao et al., 2017), and dSprites (Matthey et al., 2017). On these toy datasets we also ensure that the object is independently chosen from the background. The description and results on these artificial datasets is included in Appendix C.1.

We validate our approach on purely real datasets. The first dataset is a real side-scan sonar (SSS) dataset (Sethuraman et al., 2024), which contains a variety of foreground objects corresponding to different sites that contain shipwrecks in Lake Michigan along with ground truth segmentation masks for the shipwrecks in the seabed. The second dataset, is the Caltech-UCSD Birds-200-2011 (CUB-200-211) dataset (Wah et al., 2011), which consists of three-channel (RGB) color images of 200 species of birds on various backgrounds with segmentations.

#### 3.4.1 Side Scan Sonar with Shipwreck Objects

The first dataset is a real side-scan sonar (SSS) dataset (Sethuraman et al., 2024), which contains a variety of foreground objects corresponding to different sites that contain shipwrecks in Lake Michigan along with ground truth segmentation masks for the shipwrecks in the seabed. The SSS dataset (Sethuraman et al., 2024) contains 28 distinct shipwrecks totaling 286 high-resolution images with segmentations. The dataset is already divided 50/50 into training and test respecting the variety of sites. We further split the training data into 70% training and 30% validation.

For each sonar scene, we crop out the black strip in the middle (i.e., the blind spot directly below the sonar platform) and we flip the right side of the sonar image so that range increases consistently from right to left in images and the acoustic shadows all have the same orientation. Then, we crop 500 $128 \times 128$ images from the 143 images in the training set. We normalize each crop by its mean and then clip any value larger than 16. Then, we resample each crop to $64 \times 64$. We use ground truth labels to label each crop as composite or background-only. Although this approach uses supervised information, the idea of weak supervision is that each crop could be quickly manually labeled or one could use a statistical anomaly detection algorithm for the presence of objects in groups. In either case, these are beyond the scope of this work.

For testing, for each of the 143 test set images, we take $128 \times 128$ crops with 90%-overlap. Each crop is processed as above. The final segmentation mask is the mean across the overlapped masks. This is a convolutional approach, and the mean of the masks acts as a majority-vote segmentation, where the votes comes from the same pixel being in multiple overlapping crops.

#### 3.4.2 CUB-200-211

To illustrate the broader applicability of our approach across diverse imaging modalities, we also evaluate it on a fourth dataset comprising natural images from the CUB dataset. We also demonstrate our work on the CUB-200-211 dataset (Wah et al., 2011), which consists of 11,788 images of birds from 200 species on various backgrounds. We chose this dataset to demonstrate that our work can also be applied to natural

images, although the assumptions of independence of object and background are likely violated for birds with different habitats. Each image is min-max normalized such that all pixel values are between $[0, 1]$. We report the results for the separate testing set which consists of the half of the images, specifically, the train-test split has 5994 train and 5794 test images. We further split the training data into 70% training and 30% validation. Additionally, when benchmarking against other unsupervised object segmentation approaches, we follow Chen et al. (2019) and use their split consists of 10,000 images for training, 1,000 for testing, and the remaining 778 for validation.

### 3.5 Implementation Details

The AE or CL encoder (CLE) and K-means are trained on background-only images. The AE architecture is composed of 4 convolution layers each followed by a batch normalization layer and ReLU activation. The number of kernels in each layer is $\{64, 128, 256, 512\}$. A fully connected bottleneck layer of dimension $o = 20$ is used to represent the latent space. Similarly, the decoder is composed of one fully connected layer and 4 transpose convolutions with the same number of kernels as the encoder but with a reversed order. We add a sigmoid layer at the end of the decoder as we find it accelerates training the AE. We used the Adam optimizer to optimize the AE, with a fixed learning rate of 0.0001, and batch size of 4096. The CLE follow the exact design of the encoder part in the AE but we increased the latent dimension to $o = 200$ for CUB dataset.

For the SSS dataset, a nearby patch of seafloor without any object can be passed to the AE/CLE + Sinkhorn K-means to infer the background of a foreground object image. The entropic regularization parameter in the Sinkhorn algorithm was set to 0.01. For CUB-200-2011, we train CLE and K-means and we use patches of size 25% of the image width and height taken from the composite images as background-only images: during CLE training, we use the ground truth masks to ensure that the patch does not contain any objects, but during training of the masking network we use a random patch cropped from the input image. In this case, we use the ground truth to satisfy the assumption that representative background-only images are available; however we train the masking network without any ground truth knowledge. For the contrastive learning, we use augmentation techniques such as random cropping to assign positive pairs. We also used random horizontal flipping for the CUB dataset.

For SSS dataset, we choose clusters from the set $\{2, 3, 4, 5\}$ but we found that they perform very similarly so we only report the 4 clusters results. For CUB-200-2011, we train models with varying the number of clusters, choosing values from the set $\{5, 10, 15\}$. In both cases, the choice of cluster numbers is guided by the visual distinctiveness of example images in each cluster: we increase the number of clusters until further subdivision yields negligible improvement in visual separation.

We choose our segmentation model to be the U-Net (Ronneberger et al., 2015b) with default parameters. We choose D-adaptation optimizer to optimize U-Net (Defazio & Mishchenko, 2023). The learning rate for the U-Net is 1 and the batch size is 400. We selected the largest batch size the GPU we used for training could handle. For the SSS and CUB datasets, we run the training for 150 and 200 epochs, respectively. We choose the model with lowest validation loss $\mathcal{L}$ shown in equation 8. We implement our approach using the `PyTorch Lightning` (Falcon & The PyTorch Lightning team, 2019) framework. Only one GPU, a `Tesla V100-SXM2-32GB`, is used for training.

## 4 Results

In the main body, we present results for the real datasets, with appendices containing results on the synthetic Texture+MNIST/FashionMNIST/dSprites C.3 and SAS+dSprites C.4, additional results on real images D, and failure of benchmarks on single-channel images: C.3.1 for synthetic data and D.2 for the SSS dataset. Since our method is weakly supervised, it is noteworthy that our method achieves near-perfect performance (False Positive Rate $< 0.5\%$) for background images across all datasets and cluster numbers (except for the SSS dataset, which has its own discussion). As a result, our primary focus will be on the segmentation of foreground objects. When ground truth masks are available we evaluate the segmentation performance on composite images using the following metrics: area-under-the-curve of the receiver operating characteristic

(AUCROC), mean intersection of cardinality (IOC) (also known as Jaccard index, which is slightly more conservative than the intersection over union metric) with mask threshold at 0.5, and average precision.

### 4.1 Side Scan Sonar (SSS) Dataset

We first present visualizations of the input image, ground truth, estimated masking, and thresholded estimated masking for several images in Figure 2. We note that our mask often include more of the shadow, but the ground truth does not account for these shadows. Despite this, our model successfully recovers the ships, providing more precise segmentation in the second and third images. Further examples can be found in Figure 12 where the capturing of shadows is more pronounced. Additionally, we note that because the seabed sand moves, it may cover non-edge parts of the ships, making it reasonable for these regions to be segmented as background. This effect is even more pronounced in Figure 12, which demonstrates two key observations: first, our methodology captures the foreground shadow, an aspect not represented in the ground truth. Second, our model extracts 'foreground' objects that are not ships, such as rocks and coarse regions, as illustrated in Figure 14. Finally, in Figure 13 we show more examples of ships and small objects with relatively small shadows.

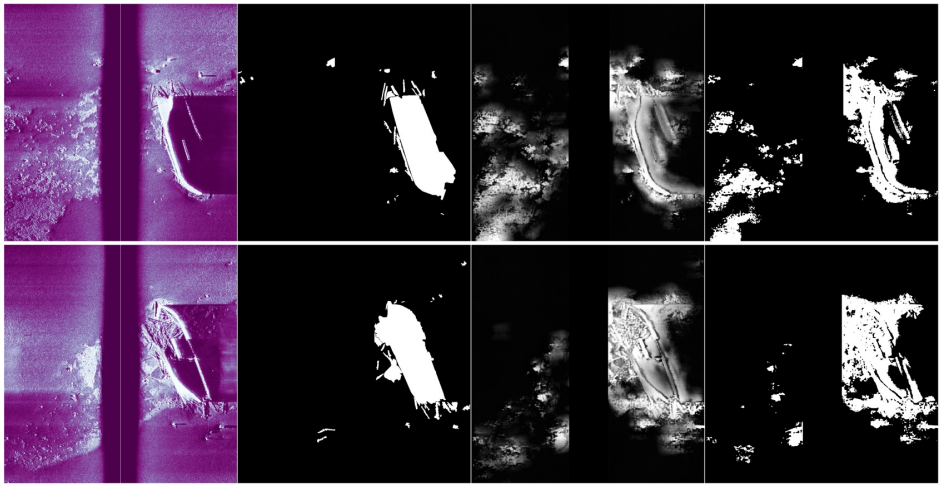

Figure 2: Segmentation model results on SSS images. Each row corresponds to a different image. From left to right: input images, ground truth masks, estimated masks, and thresholded estimated masks at 0.5. Images sites: Lucinda van Valkenburg.

#### 4.1.1 Performance against Supervised Baselines

Given that our segmentation method includes additional foreground objects (e.g., rocks), captures shadows, and ignores portions of wrecks covered by sand—elements not considered in the ground truth—we believe a direct comparison with the provided ground truth may not fully reflect the model's performance. Nonetheless, we benchmark our method against supervised methods selected to reflect the variety of deep learning-based segmentation models used in the vision community: Yang (Yang et al., 2022a), ViT Adapter (Chen et al., 2022), DeepLabV3 (Chen et al., 2017), HRNet (Wang et al., 2020), U-Net (Ronneberger et al., 2015a), and Salient Object Detection, InSPyReNet (Kim et al., 2023). Following (Sethuraman et al., 2024), we aggregate the images per site and report the IOC for each cite in Table 1. Our unsupervised method has comparable or superior average performance to 4 supervised methods, but is outperformed by supervised U-Net and SOD. We also note that across the sites our performance co-varies with the best method. We outperform other methods on sites where the supervised methods also fail. For example, on the 'James Davidson' site, one portion shown in Figure 15, false alarms are evident, where parts of the background are incorrectly identified as foreground, with no clear rationale behind these misclassifications. We believe this issue arises because the models have not encountered such a background during training and, as a result, mistakenly segment it.

| Site | Yang | ViT-Adapter | DeepLabv3 | HRNet | U-Net | SOD | Ours | Our rank |
|---|---|---|---|---|---|---|---|---|
| Artificial Reef | 0.002 | 0.003 | 0.003 | 0.011 | 0.006 | 0.017 | **0.05** | 1 |
| Barge | 0.471 | 0.412 | 0.670 | 0.703 | 0.736 | **0.775** | 0.52 | 5 |
| Corsair | 0.231 | 0.542 | 0.531 | 0.293 | 0.564 | **0.583** | 0.43 | 5 |
| Corsican | 0.056 | 0.088 | 0.042 | **0.174** | 0.116 | 0.077 | 0.162 | 2 |
| James Davidson | 0.000 | 0.000 | 0.031 | 0.067 | 0.074 | 0.091 | **0.092** | 1 |
| WH Gilbert | 0.276 | 0.006 | 0.658 | 0.641 | 0.726 | **0.749** | 0.623 | 5 |
| Haltiner Barge | 0.031 | 0.368 | **0.459** | 0.448 | 0.242 | 0.442 | 0.357 | 5 |
| Lucinda van Valkenburg | 0.367 | 0.127 | 0.645 | 0.641 | 0.641 | **0.713** | 0.542 | 5 |
| Monohansett | 0.020 | **0.496** | 0.034 | 0.207 | 0.042 | 0.467 | 0.361 | 3 |
| Monrovia | 0.478 | 0.469 | 0.411 | 0.566 | 0.572 | **0.572** | 0.487 | 4 |
| Shamrock | 0.102 | 0.354 | 0.151 | 0.003 | **0.428** | 0.001 | 0.143 | 4 |
| WP Thew | 0.161 | 0.176 | 0.419 | 0.437 | 0.545 | **0.580** | 0.391 | 5 |
| Viator | 0.563 | 0.631 | 0.667 | 0.646 | 0.646 | **0.776** | 0.521 | 7 |
| Average | 0.21±0.20 | 0.28±0.22 | 0.36±0.27 | 0.37±0.26 | 0.41±0.28 | 0.45±0.30 | 0.36±0.19 | 4.00±1.78 |

Table 1: Per-site IoC comparison between our method and supervised benchmark baselines. Bold indicates the best performance per site.

#### 4.1.2 Unsupervised Segmentation Benchmarks

We attempted to apply unsupervised object segmentation methods introduced by Zou et al. (2023); Chen et al. (2019); Savarese et al. (2021) as benchmarks for the Side Scan Sonar with Shipwreck Objects. We choose ILSGAN (Zou et al., 2023) as it is the best performing method among the generative-based methods, ReDO (Chen et al., 2019) as it makes the minimal assumption about the foreground objects (e.g., it does not assume a minimal object size), and finally the work by Savarese et al. (2021) for its unique attributes (i.e., no pre-trained models, no adversarial training, and no need for data labels).

We use the same pre-processing steps explained in Section 3.4.1 with the same patch size. We adapt the model architectures to accept one channel instead of three. We also use the same hyperparameters used by the authors. We found that the networks produce either trivial masks (i.e., all ones or all zeros) or masks without any meaningful segmentation. The work ReDo by Chen et al. (2019) converged to either almost all-zero masks or all-ones masks as shown in Figure 16 in the appendix. The foreground mask typically contains either diffuse low-intensity values or small, high-intensity regions. These mask patterns appear to be leveraged by the model to promote statistical dependency—i.e., mutual information—between the input noise vector and the resulting generated image. We use their default setting of generating two masks. Additionally, to ensure a fair comparison, we also tried adding a supervised loss for background-only images, the mean squared loss for the generated mask, which is minimized if the generated mask is all zeros, as in equation 7. Figure 17 shows examples for background and composite patches where our MSE loss drives the foreground mask to be completely all-zeros.

For ILSGAN (Zou et al., 2023), the trained model was able to generate realistic images; however, the corresponding masks almost all zero. In other words, the model degenerates and ignores the possible presence of the shipwreck objects shown in Figure 18 in the appendix. This is not surprising as the 'foreground' is very similar to the background.

Finally, we attempted to use the method by Savarese et al. (2021), since it is a model-free method, we applied two schemes: the first one is to input the whole sonar image and the second one use a patch-based scheme with 50% overlap. However, both schemes provide nonsensical masks as expected for an unsupervised method designed to work on color images with the object at the center. Results are shown in Figure 19 in the appendix. Although we show only two examples, this observation is consistent across the testing images.

Admittedly, the hyperparameters selected in prior work, which work when trained on colored natural images, may not be optimal; however, for unsupervised segmentation it is not clear how to conduct the required hyperparameter search. Even with the weak supervision, we hypothesize that these methods may simply be poorly suited for single channel images, such as sonar images, that lack the color and optical cues of foreground and background found in natural imagery. To test this hypothesis, in addition to sonar images, we also benchmark some other works using our synthetic datasets (see C.3).

### 4.2 CUB Dataset

To qualitatively assess segmentation performance, we show 16 images from the testing set along with their segmentations and the birds masks in Figure 3.

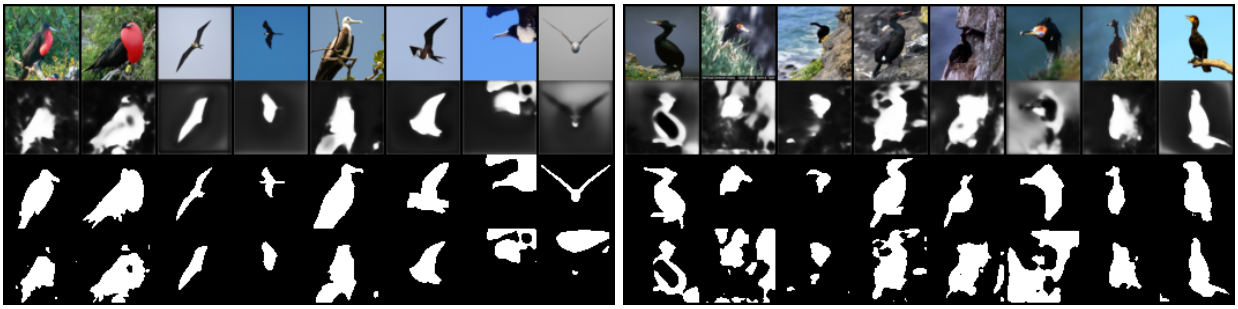

Figure 3: Results of the segmentation model for CUB. From top to bottom: input images, estimated masks, true masks, and thresholded estimated masks at .5.

In Figure 4, we show a variety of counterfactual images. We notice that the majority of the generated counterfactual images do look like real images. However, there are interesting cases where the masking network, in addition to birds, captures other objects. For example, it captures tree branches (e.g., third row, 6th and 7th columns), rocks (e.g., third row, 14th column), wires (first row, last column), cars (first row, 8th column). These objects can be still considered as foreground, so capturing them is not surprising. Also, we can see some unexplained failure such as the 10th and 12th pictures in the first row, where for the former the counterfactual does not appear to differ from the input image and for the latter, the counterfactual does not look like anything in the CUB dataset.

Figure 4: Generated counterfactual images based on test images using 10 clusters. Each block is composed of two rows and 8 columns. Each block shows the original input images in the first row and the corresponding counterfactual images in the second row. The counterfactual are created by alpha-blending the real input images with randomly selected backgrounds. Each second row in the blocks should ideally be composed of the same background clusters. An example of the obtained clusters is shown in Figure 21 in the appendix.

To delve into more examples, we show the generated counterfactual images using the corresponding source composite images (first column) and the source background images (first row) in Figure 20 in the appendix.

For quantitative results, we show in Table 2 the mean IOC metric for different cluster numbers under AE+K-means and CL+K-means settings (other metrics are in Table 6).

We also show masking results and counterfactual images generated by the masking network trained using background clusters obtained from CL+Kmeans and AE+Kmeans for different numbers of clusters in Figures **??**, **??**, and **??** in the appendix.

Table 2: Masking Network Performance (mean IoC) Comparison of AE+K-means and CL+K-Means based Background Clustering.

| Number of Clusters | AE+K-means | CL+K-means |
|---|---|---|
| 5 | 20% | **30**% |
| 10 | 24% | **30**% |
| 15 | 24% | **26**% |

#### 4.2.1 Benchmark Comparison

We also include a comparison between our method and other related work that does not require pretrained networks as in Table 3. Here, we use a 5 cluster method. The model is different than the one previously discussed, as the benchmark (Chen et al., 2019) uses more training data, i.e., 10,000 instances compared to the approx. 5,000 instances used in Table2. With the additional training data, our mean IoC performance increases by 6 percentage points.

Table 3: IoC scores on the CUB dataset across different methods. Bold indicates the best score. From left to right, each work corresponds to Singh et al. (2019), Chen et al. (2019),Bielski & Favaro (2019),Hung et al. (2019),Savarese et al. (2021),Yang et al. (2022b), He et al. (2022), Zou et al. (2023), respectively.

| FineGAN | ReDO | PerturbGAN | SCOPS | Savarse et al. | Yang et al. | GANSeg | ILSGAN | Ours |
|---|---|---|---|---|---|---|---|---|
| 44.5 | 42.6 | 38.0 | 32.9 | 55.1 | 69.7 | 62.9 | **72.1** | 35.6 |

## 5 Discussion

We introduced a framework for weakly-supervised foreground object segmentation within a dataset comprising both foreground and background images. Our approach leverages background images to formulate a straightforward loss function that avoids degenerate solutions and offers a more straightforward training scheme compared to generative and ViT-based models. Our approach can be applied without relying on large models pretrained on natural imagery. Methods based on such models often cannot be directly applied to other data modalities. However, our approach can be directly applied to other modalities such as sonar object data. The distinctive combination of our dataset and framework sets our work apart.

We demonstrate the limitations of related work by applying two works by Bielski & Favaro (2019) and Xie et al. (2022) to our synthetic datasets. Both methods failed to converge to a solution where the segmentation results are acceptable. This is due to the lack of a well-pretrained model (for the work done by Xie et al. (2022)) and having diverse classes of foreground objects (for the work done by Bielski & Favaro (2019)).

In addition to sonar data, we also demonstrate relatively good performance on natural images using the CUB dataset. During training of the masking network, random patches are taken from the input image to assign a background cluster for the conditional divergence loss. This demonstrates that our approach can also be used for datasets composed only of composite images (as long as the images are not tightly cropped around the objects).

Although one of the main contributions of our work is the avoidance of pretrained models, they can be used to extract reliable initial heuristic cues of where the foreground object is. This can be useful in extracting background patches that are used to train the clustering AE or to help guide the masking network.

The main limitation of our approach is the reliance on an appropriate background clustering. Although we observe that synthetic and CUB dataset achieves relatively similar performance with a different number of clusters constructed under varying settings, we believe the quality of the background clusters is crucial for our method to work. This is more pronounced in sonar dataset, where we have noticed a failure mode for K-means in which it assigns the vast majority of instances to a single cluster. In this case, we had to discourage it from doing so by using Sinkhorn algorithm. Selecting the correct approach to clustering can be a challenging task. Notably, the clustering does not have to correspond to true background classes.

## References


Avi Abu and Roee Diamant. Unsupervised segmentation of underwater objects in sonar images. *OCEANS 2017-Aberdeen*, pp. 1–5, 2017.

Avi Abu and Roee Diamant. Unsupervised local spatial mixture segmentation of underwater objects in sonar images. *IEEE Journal of Oceanic Engineering*, 44(4):1179–1197, 2018.

Martin Arjovsky, Soumith Chintala, and Léon Bottou. Wasserstein generative adversarial networks. In *International Conference on Machine Learning*, pp. 214–223. PMLR, 2017.

Spyridon Bakas, Hamed Akbari, Aristeidis Sotiras, Michel Bilello, Martin Rozycki, Justin S Kirby, John B Freymann, Keyvan Farahani, and Christos Davatzikos. Advancing the cancer genome atlas glioma MRI collections with expert segmentation labels and radiomic features. *Scientific Data*, 4(1):1–13, 2017.

Jonathan T Barron and Ben Poole. The fast bilateral solver. In *European Conference on Computer Vision*, pp. 617–632. Springer, 2016.

Claude Bélisle, Jean-Claude Massé, and Thomas Ransford. When is a probability measure determined by infinitely many projections? *The Annals of Probability*, 25(2):767 – 786, 1997. doi: 10.1214/aop/1024404418. URL `https://doi.org/10.1214/aop/1024404418`.

Adam Bielski and Paolo Favaro. Emergence of object segmentation in perturbed generative models. *Advances in Neural Information Processing Systems*, 32, 2019.

Felix Biggs, Antonin Schrab, and Arthur Gretton. Mmd-fuse: Learning and combining kernels for two-sample testing without data splitting. *Advances in Neural Information Processing Systems*, 36:75151–75188, 2023.

Phil Brodatz. *Textures: A Photographic Album for Artists and Designers*. Dover Publications, New York, 1966.

Jingwei Cao, Hongyu Zhang, Lisheng Jin, Jiawang Lv, Guoyang Hou, and Chengtao Zhang. A review of object tracking methods: From general field to autonomous vehicles. *Neurocomputing*, pp. 127635, 2024.

Mathilde Caron, Hugo Touvron, Ishan Misra, Hervé Jégou, Julien Mairal, Piotr Bojanowski, and Armand Joulin. Emerging properties in self-supervised vision transformers. In *Proceedings of the IEEE/CVF International Conference on Computer Vision*, pp. 9650–9660, 2021.

Yu-Ting Chang, Qiaosong Wang, Wei-Chih Hung, Robinson Piramuthu, Yi-Hsuan Tsai, and Ming-Hsuan Yang. Weakly-supervised semantic segmentation via sub-category exploration. In *Proceedings of the IEEE/CVF Conference on Computer Vision and Pattern Recognition*, pp. 8991–9000, 2020.

Liang-Chieh Chen, George Papandreou, Florian Schroff, and Hartwig Adam. Rethinking Atrous Convolution for Semantic Image Segmentation. *arXiv*, June 2017. doi: 10.48550/arXiv.1706.05587.

Mickaël Chen, Thierry Artières, and Ludovic Denoyer. Unsupervised Object Segmentation by Redrawing. *Advances in Neural Information Processing Systems*, 32, 2019. URL `https://proceedings.neurips.cc/paper_files/paper/2019/hash/32bbf7b2bc4ed14eb1e9c2580056a989-Abstract.html`.

Xiaoran Chen and Ender Konukoglu. Unsupervised detection of lesions in brain MRI using constrained adversarial auto-encoders. *arXiv preprint arXiv:1806.04972*, 2018.

Zhe Chen, Yuchen Duan, Wenhai Wang, Junjun He, Tong Lu, Jifeng Dai, and Yu Qiao. Vision Transformer Adapter for Dense Predictions. *arXiv*, May 2022. doi: 10.48550/arXiv.2205.08534.

Pengyu Cheng, Weituo Hao, Shuyang Dai, Jiachang Liu, Zhe Gan, and Lawrence Carin. Club: A contrastive log-ratio upper bound of mutual information. In *International Conference on Machine Learning*, pp. 1779–1788. PMLR, 2020.

James T. Cobb and Alina Zare. Boundary detection and superpixel formation in synthetic aperture sonar imagery. In *3rd Int. Conf. SAS and SAR*, Sept. 2014.

Marco Cuturi. Sinkhorn distances: Lightspeed computation of optimal transport. *Advances in Neural Information Processing Systems*, 26, 2013.

Aaron Defazio and Konstantin Mishchenko. Learning-rate-free learning by d-adaptation. *The 40th International Conference on Machine Learning (ICML 2023)*, 2023.

Ishan Deshpande, Ziyu Zhang, and Alexander G Schwing. Generative modeling using the sliced Wasserstein distance. In *Proceedings of the IEEE Conference on Computer Vision and Pattern Recognition*, pp. 3483–3491, 2018.

Ishan Deshpande, Yuan-Ting Hu, Ruoyu Sun, Ayis Pyrros, Nasir Siddiqui, Sanmi Koyejo, Zhizhen Zhao, David Forsyth, and Alexander G Schwing. Max-sliced Wasserstein distance and its use for GANs. In *Proceedings of the IEEE Conference on Computer Vision and Pattern Recognition*, pp. 10648–10656, 2019.

Alexey Dosovitskiy, Lucas Beyer, Alexander Kolesnikov, Dirk Weissenborn, Xiaohua Zhai, Thomas Unterthiner, Mostafa Dehghani, Matthias Minderer, Georg Heigold, Sylvain Gelly, Jakob Uszkoreit, and Neil Houlsby. An image is worth 16x16 words: Transformers for image recognition at scale, 2021.

William Falcon and The PyTorch Lightning team. PyTorch Lightning, March 2019. URL `https://github.com/Lightning-AI/lightning`.

Haoxiang Gao, Zhongruo Wang, Yaqian Li, Kaiwen Long, Ming Yang, and Yiqing Shen. A survey for foundation models in autonomous driving. *arXiv preprint arXiv:2402.01105*, 2024.

Ian Goodfellow, Jean Pouget-Abadie, Mehdi Mirza, Bing Xu, David Warde-Farley, Sherjil Ozair, Aaron Courville, and Yoshua Bengio. Generative adversarial nets. *Advances in Neural Information Processing Systems*, 27, 2014.

Mark Hamilton, Zhoutong Zhang, Bharath Hariharan, Noah Snavely, and William T Freeman. Unsupervised semantic segmentation by distilling feature correspondences. *arXiv preprint arXiv:2203.08414*, 2022.

Xingzhe He, Bastian Wandt, and Helge Rhodin. Ganseg: Learning to segment by unsupervised hierarchical image generation. In *Proceedings of the IEEE/CVF Conference on Computer Vision and Pattern Recognition*, pp. 1225–1235, 2022.

Qibin Hou, PengTao Jiang, Yunchao Wei, and Ming-Ming Cheng. Self-erasing network for integral object attention. *Advances in Neural Information Processing Systems*, 31, 2018.

Wei-Chih Hung, Varun Jampani, Sifei Liu, Pavlo Molchanov, Ming-Hsuan Yang, and Jan Kautz. Scops: Self-supervised co-part segmentation. In *IEEE Conf. on Computer Vision and Pattern Recognition (CVPR)*, 2019.

Saghar Irandoust, Thibaut Durand, Yunduz Rakhmangulova, Wenjie Zi, and Hossein Hajimirsadeghi. Training a vision transformer from scratch in less than 24 hours with 1 GPU. *arXiv preprint arXiv:2211.05187*, 2022.

Peng-Tao Jiang, Qibin Hou, Yang Cao, Ming-Ming Cheng, Yunchao Wei, and Hong-Kai Xiong. Integral object mining via online attention accumulation. In *Proceedings of the IEEE/CVF Conference on Computer Vision and Pattern Recognition*, pp. 2070–2079, 2019.

Devanish N Kamtam, Joseph B Shrager, Satya Deepya Malla, Nicole Lin, Juan J Cardona, Jake J Kim, and Clarence Hu. Deep learning approaches to surgical video segmentation and object detection: A scoping review. *arXiv preprint arXiv:2502.16459*, 2025.

Taehun Kim, Kunhee Kim, Joonyeong Lee, Dongmin Cha, Jiho Lee, and Daijin Kim. Revisiting Image Pyramid Structure for High Resolution Salient Object Detection. In *Computer Vision – ACCV 2022*, pp. 257–273. Springer, Cham, Switzerland, March 2023. ISBN 978-3-031-26293-7. doi: 10.1007/978-3-031-26293-7_16.

Soheil Kolouri, Gustavo K Rohde, and Heiko Hoffmann. Sliced Wasserstein distance for learning Gaussian mixture models. In *Proceedings of the IEEE Conference on Computer Vision and Pattern Recognition*, pp. 3427–3436, 2018.

Krishna Kumar Singh and Yong Jae Lee. Hide-and-seek: Forcing a network to be meticulous for weakly-supervised object and action localization. In *Proceedings of the IEEE International Conference on Computer Vision*, pp. 3524–3533, 2017.

John Lafferty, Andrew McCallum, Fernando Pereira, et al. Conditional random fields: Probabilistic models for segmenting and labeling sequence data. In *ICMLß*, volume 1, pp. 3. Williamstown, MA, 2001.

Ho Hin Lee, Yu Gu, Theodore Zhao, Yanbo Xu, Jianwei Yang, Naoto Usuyama, Cliff Wong, Mu Wei, Bennett A Landman, Yuankai Huo, et al. Foundation models for biomedical image segmentation: A survey. *arXiv preprint arXiv:2401.07654*, 2024.

Seungho Lee, Minhyun Lee, Jongwuk Lee, and Hyunjung Shim. Railroad is not a train: Saliency as pseudo-pixel supervision for weakly supervised semantic segmentation. In *Proceedings of the IEEE/CVF Conference on Computer Vision and Pattern Recognition*, pp. 5495–5505, 2021.

Chun-Liang Li, Wei-Cheng Chang, Yu Cheng, Yiming Yang, and Barnabás Póczos. MMD GAN: Towards deeper understanding of moment matching network. *Advances in neural information processing systems*, 30, 2017.

Kunpeng Li, Ziyan Wu, Kuan-Chuan Peng, Jan Ernst, and Yun Fu. Tell me where to look: Guided attention inference network. In *Proceedings of the IEEE Conference on Computer Vision and Pattern Recognition*, pp. 9215–9223, 2018.

Xiang Li, Chung-Ching Lin, Yinpeng Chen, Zicheng Liu, Jinglu Wang, and Bhiksha Raj. Paintseg: Training-free segmentation via painting. *arXiv preprint arXiv:2305.19406*, 2023.

Jun Ma, Yuting He, Feifei Li, Lin Han, Chenyu You, and Bo Wang. Segment anything in medical images. *Nature Communications*, 15(1):654, 2024.

Zdravko Marinov, Paul F Jäger, Jan Egger, Jens Kleesiek, and Rainer Stiefelhagen. Deep interactive segmentation of medical images: A systematic review and taxonomy. *IEEE Transactions on Pattern Analysis and Machine Intelligence*, 2024.

Loic Matthey, Irina Higgins, Demis Hassabis, and Alexander Lerchner. dsprites: Disentanglement testing sprites dataset. https://github.com/deepmind/dsprites-dataset/, 2017.

Khai Nguyen and Nhat Ho. Energy-based sliced wasserstein distance. *Advances in Neural Information Processing Systems*, 36:18046–18075, 2023.

Sebastian Nowozin, Botond Cseke, and Ryota Tomioka. f-gan: Training generative neural samplers using variational divergence minimization. *Advances in neural information processing systems*, 29, 2016.

Pavel Ostyakov, Roman Suvorov, Elizaveta Logacheva, Oleg Khomenko, and Sergey I Nikolenko. Seigan: Towards compositional image generation by simultaneously learning to segment, enhance, and inpaint. *arXiv preprint arXiv:1811.07630*, 2018.

Nobuyuki Otsu. A threshold selection method from gray-level histograms. *IEEE Transactions on Systems, Man, and Cybernetics*, 9(1):62–66, 1979.

Alan Preciado-Grijalva, Bilal Wehbe, Miguel Bande Firvida, and Matias Valdenegro-Toro. Self-supervised learning for sonar image classification. In *Proceedings of the IEEE/CVF Conference on Computer Vision and Pattern Recognition*, pp. 1499–1508, 2022.

Tal Remez, Jonathan Huang, and Matthew Brown. Learning to segment via cut-and-paste. In *Proceedings of the European Conference on Computer Vision (ECCV)*, pp. 37–52, 2018.

Robin Rombach, Andreas Blattmann, Dominik Lorenz, Patrick Esser, and Björn Ommer. High-resolution image synthesis with latent diffusion models. In *Proceedings of the IEEE/CVF Conference on Computer Vision and Pattern Recognition*, pp. 10684–10695, 2022.

Olaf Ronneberger, Philipp Fischer, and Thomas Brox. U-Net: Convolutional Networks for Biomedical Image Segmentation. In *Medical Image Computing and Computer-Assisted Intervention – MICCAI 2015*, pp. 234–241. Springer, Cham, Switzerland, November 2015a. ISBN 978-3-319-24574-4. doi: 10.1007/978-3-319-24574-4_28.

Olaf Ronneberger, Philipp Fischer, and Thomas Brox. U-net: Convolutional networks for biomedical image segmentation. In *Medical Image Computing and Computer-Assisted Intervention–MICCAI 2015: 18th International Conference, Munich, Germany, October 5-9, 2015, Proceedings, Part III 18*, pp. 234–241. Springer, 2015b.

Olga Russakovsky, Jia Deng, Hao Su, Jonathan Krause, Sanjeev Satheesh, Sean Ma, Zhiheng Huang, Andrej Karpathy, Aditya Khosla, Michael Bernstein, et al. Imagenet large scale visual recognition challenge. *International Journal of Computer Vision*, 115:211–252, 2015.

Filippo Santambrogio. Optimal transport for applied mathematicians. *Birkäuser, NY*, 55(58-63):94, 2015.

Sauer and Geiger. Counterfactual generative networks. In *International Conference on Learning Representations (ICLR)*, 2021.

Pedro Savarese, Sunnie SY Kim, Michael Maire, Greg Shakhnarovich, and David McAllester. Information-theoretic segmentation by inpainting error maximization. In *Proceedings of the IEEE/CVF Conference on Computer Vision and Pattern Recognition*, pp. 4029–4039, 2021.

Advaith V Sethuraman, Anja Sheppard, Onur Bagoren, Christopher Pinnow, Jamey Anderson, Timothy C Havens, and Katherine A Skinner. Machine learning for shipwreck segmentation from side scan sonar imagery: Dataset and benchmark. *The International Journal of Robotics Research*, pp. 02783649241266853, 2024.

Jianbo Shi and Jitendra Malik. Normalized cuts and image segmentation. *IEEE Transactions on Pattern Analysis and Machine Intelligence*, 22(8):888–905, 2000.

Krishna Kumar Singh, Utkarsh Ojha, and Yong Jae Lee. Finegan: Unsupervised hierarchical disentanglement for fine-grained object generation and discovery. In *CVPR*, 2019.

Kihyuk Sohn, David Berthelot, Nicholas Carlini, Zizhao Zhang, Han Zhang, Colin A Raffel, Ekin Dogus Cubuk, Alexey Kurakin, and Chun-Liang Li. Fixmatch: Simplifying semi-supervised learning with consistency and confidence. *Advances in Neural Information Processing Systems*, 33:596–608, 2020.

Ziying Song, Lin Liu, Feiyang Jia, Yadan Luo, Caiyan Jia, Guoxin Zhang, Lei Yang, and Li Wang. Robustness-aware 3d object detection in autonomous driving: A review and outlook. *IEEE Transactions on Intelligent Transportation Systems*, 2024.

Yung-Chen Sun, Isaac D Gerg, and Vishal Monga. Iterative, deep synthetic aperture sonar image segmentation. *IEEE Transactions on Geoscience and Remote Sensing*, 60:1–15, 2022.

Matias Valdenegro-Toro, Alan Preciado-Grijalva, and Bilal Wehbe. Pre-trained models for sonar images. In *OCEANS 2021: San Diego–Porto*, pp. 1–8. IEEE, 2021.

Cédric Villani et al. *Optimal transport: old and new*, volume 338. Springer, 2008.

Catherine Wah, Steve Branson, Peter Welinder, Pietro Perona, and Serge Belongie. The caltech-ucsd birds-200-2011 dataset. 2011.

Jingdong Wang, Ke Sun, Tianheng Cheng, Borui Jiang, Chaorui Deng, and Yang Zhao. Deep High-Resolution Representation Learning for Visual Recognition. *IEEE Trans. Pattern Anal. Mach. Intell.*, 43(10):3349–3364, April 2020. doi: 10.1109/TPAMI.2020.2983686.

Xudong Wang, Rohit Girdhar, Stella X Yu, and Ishan Misra. Cut and learn for unsupervised object detection and instance segmentation. In *Proceedings of the IEEE/CVF Conference on Computer Vision and Pattern Recognition*, pp. 3124–3134, 2023a.

Yangtao Wang, Xi Shen, Yuan Yuan, Yuming Du, Maomao Li, Shell Xu Hu, James L Crowley, and Dominique Vaufreydaz. Tokencut: Segmenting objects in images and videos with self-supervised transformer and normalized cut. *IEEE Transactions on Pattern Analysis and Machine Intelligence*, 2023b.

Chengwei Wei, Yunfei Bai, Chang Liu, Yuhe Zhu, Caiju Wang, and Xiaomao Li. Unsupervised underwater shipwreck detection in side-scan sonar images based on domain-adaptive techniques. *Scientific Reports*, 14(1):12687, 2024.

Yunchao Wei, Jiashi Feng, Xiaodan Liang, Ming-Ming Cheng, Yao Zhao, and Shuicheng Yan. Object region mining with adversarial erasing: A simple classification to semantic segmentation approach. In *Proceedings of the IEEE Conference on Computer Vision and Pattern Recognition*, pp. 1568–1576, 2017.

Jiqing Wu, Zhiwu Huang, Dinesh Acharya, Wen Li, Janine Thoma, Danda Pani Paudel, and Luc Van Gool. Sliced Wasserstein generative models. In *Proceedings of the IEEE Conference on Computer Vision and Pattern Recognition*, pp. 3713–3722, 2019.

Tong Wu, Junshi Huang, Guangyu Gao, Xiaoming Wei, Xiaolin Wei, Xuan Luo, and Chi Harold Liu. Embedded discriminative attention mechanism for weakly supervised semantic segmentation. In *Proceedings of the IEEE/CVF Conference on Computer Vision and Pattern Recognition*, pp. 16765–16774, 2021.

Han Xiao, Kashif Rasul, and Roland Vollgraf. Fashion-mnist: a novel image dataset for benchmarking machine learning algorithms. *arXiv preprint arXiv:1708.07747*, 2017.

Jinheng Xie, Jianfeng Xiang, Junliang Chen, Xianxu Hou, Xiaodong Zhao, and Linlin Shen. C2AM: Contrastive learning of class-agnostic activation map for weakly supervised object localization and semantic segmentation. In *Proceedings of the IEEE/CVF Conference on Computer Vision and Pattern Recognition*, pp. 989–998, 2022.

Lian Xu, Wanli Ouyang, Mohammed Bennamoun, Farid Boussaid, and Dan Xu. Multi-class token transformer for weakly supervised semantic segmentation. In *Proceedings of the IEEE/CVF Conference on Computer Vision and Pattern Recognition*, pp. 4310–4319, 2022.

Dianyu Yang, Chensheng Cheng, Can Wang, Guang Pan, and Feihu Zhang. Side-Scan Sonar Image Segmentation Based on Multi-Channel CNN for AUV Navigation. *Front. Neurorob.*, 16:928206, July 2022a. ISSN 1662-5218. doi: 10.3389/fnbot.2022.928206.

Yu Yang, Hakan Bilen, Qiran Zou, Wing Yin Cheung, and Xiangyang Ji. Learning foreground-background segmentation from improved layered GANs. In *Proceedings of the IEEE/CVF Winter Conference on Applications of Computer Vision*, pp. 2524–2533, 2022b.

Zhiwei Yang, Jianhu Zhao, Yongcan Yu, and Chao Huang. A sample augmentation method for side-scan sonar full-class images that can be used for detection and segmentation. *IEEE Transactions on Geoscience and Remote Sensing*, 2024.

KC Yao, Max Mignotte, Christophe Collet, Pascal Galerne, and Gilles Burel. Unsupervised segmentation using a self-organizing map and a noise model estimation in sonar imagery. *Pattern Recognition*, 33(9): 1575–1584, 2000.

Xiaolin Zhang, Yunchao Wei, Jiashi Feng, Yi Yang, and Thomas S Huang. Adversarial complementary learning for weakly supervised object localization. In *Proceedings of the IEEE Conference on Computer Vision and Pattern Recognition*, pp. 1325–1334, 2018.

Sijie Zhu, Zhe Lin, Scott Cohen, Jason Kuen, Zhifei Zhang, and Chen Chen. Topnet: Transformer-based object placement network for image compositing. In *Proceedings of the IEEE/CVF Conference on Computer Vision and Pattern Recognition*, pp. 1838–1847, 2023.

Qiran Zou, Yu Yang, Wing Yin Cheung, Chang Liu, and Xiangyang Ji. ILSGAN: Independent layer synthesis for unsupervised foreground-background segmentation. 37(9):11488–11496, 2023.

# A Literature Review

State-of-the-art approaches in unsupervised object segmentation area can be divided into three main categories—the first is generative-based (e.g., GANs), the second is based on vision transformers (ViT), and the third is class activation map (CAM). Table 4 summarizes approaches based on their reliance on pretrained models, GAN training—which can create unstable learning dynamics— object class labels, and extensive hyperparameter tuning to balance composite losses.

Table 4: Literature Review on Weakly Supervised Foreground Object Segmentation: All of the reviewed work, depends on at least one undesired attributes (pretrained model, GAN training, data labels, Extensive Hyperparameters) that hinders applying them to data-scarce domains such as sonar images.

| Category | Reference | Pretrained Models | GAN Training | Data Labels | Extensive Hyperparameters |
|---|---|---|---|---|---|
| **Generative-based** | Remez et al. (2018) | ✓ | ✓ | | ✓ |
| | Ostyakov et al. (2018) | | ✓ | | ✓ |
| | Bielski & Favaro (2019) | | ✓ | | ✓ |
| | Chen et al. (2019) | | ✓ | | |
| | Singh et al. (2019) | | ✓ | | ✓ |
| | He et al. (2022) | | ✓ | | ✓ |
| | Yang et al. (2022b) | | ✓ | | ✓ |
| | Zou et al. (2023) | | ✓ | | ✓ |
| | Sauer & Geiger (2021) | ✓ | ✓ | | ✓ |
| | Li et al. (2023) | ✓ | | | |
| **Vision-Transformers** | Dosovitskiy et al. (2021) | ✓ | | | |
| | Hamilton et al. (2022) | ✓ | | | |
| | Wang et al. (2023b) | ✓ | | | |
| **CAM-based** | Zhang et al. (2018) | ✓ | | ✓ | |
| | Li et al. (2018) | ✓ | | ✓ | ✓ |
| | Hou et al. (2018) | ✓ | | ✓ | |
| | Jiang et al. (2019) | ✓ | | ✓ | |
| | Chang et al. (2020) | ✓ | | ✓ | |
| | Lee et al. (2021) | ✓ | | ✓ | |
| | Wu et al. (2021) | ✓ | | ✓ | |
| | Xu et al. (2022) | ✓ | | ✓ | |
| | Xie et al. (2022) | ✓ | | ✓ | |
| **Others** | Hung et al. (2019) | ✓ | | | ✓ |
| | Savarese et al. (2021) | | | | ✓ |

## A.1 Generative-based Models

The work by Remez et al. (2018) is similar to ours in that it proposes a weakly-supervised approach that relies on a discriminator to assess the statistical similarity between synthetic images with counterfactual backgrounds and real images. Notably, their discriminator relies on a pretrained object classifier. Furthermore, the masking network input is based on the features from a pretrained object recognition network which outputs a bounding box for the foreground object. The necessity of using pretrained models and a network to generate a bounding box are the main limitations of this work.

Ostyakov et al. (2018) proposed a generative adversarial network (GAN) that takes a composite image as input and inpaints the foreground region with a background consistent with the original background. Subsequently, the segmented object is pasted onto a different background to generate a counterfactual image. Their model involves a segmentation network that aims to produce inpainted and counterfactual images realistic enough to deceive the discriminator. In addition to two discriminator networks, their architecture includes three auxiliary networks: a segmentation network, an inpainting network, and an enhancement

network—the latter designed to correct artifacts resulting from inaccurate object masking. To avoid trivial segmentation masks, the first discriminator distinguishes between inpainted composites and real background images, while the second discriminator differentiates counterfactual images from genuine composite images. Their total loss is extremely complicated; it consists of 11 different losses.

Bielski & Favaro (2019) proposed a GAN-based, unsupervised approach to segment foreground pixels. The GAN produces mask, foreground, and background images. The mask is used to alpha-blend the background and foreground back together. Trivial solutions for this work result when (i) the generated background and foreground are identical, so any arbitrary mask would still give a real image, (ii) Either the foreground or the background is ignored (i.e., all-foreground or all-background), which results in an either all-zero or all-one mask. To prevent the latter, the hinge loss on the average mask value is deployed. To prevent the former, a small random spatial shift of the composite image and mask are applied before alpha-blending to create a counterfactual shift in the resulting synthetic image. This shift penalizes having poor generated masks with identical foreground and background by creating a statistical divergence between shifted counterfactuals (i.e., the generated image) and real images, which the discriminator can detect. A drawback to this approach is the number of different loss functions (size, binary, gradient penalty, discriminator output norm) and hyper-parameters required to prevent degenerate solutions.

Building on the layered-GAN approach of the previous work (Bielski & Favaro, 2019), the method by Yang et al. (2022b), used more general perturbations of mask and foreground via affine transforms and added mutual information objectives between the random codes for foreground generation and the resulting mask and synthetic image. There are two random codes for the two GANs (GAN-1 and GAN-2). The first code is shared and used by GAN-1 for generating backgrounds and GAN-2 for generating foregrounds and masks in conjunction with the second code which is used only by GAN-2. Maximizing the mutual information between the rendered synthetic image and the second code prevents producing all-zero masks—if the mask is all-zeros then the image will be equivalent to the generated background image which has zero mutual information with the second code. On the other hand, maximizing the mutual information between the mask and the second code encourages mixed-value masks (i.e., variety of zeros and ones). The reason behind this is that since the map is deterministic, the mutual information is equivalent to the entropy of the mask. Finally, a masking network is jointly trained based on the data generated by the GAN model. This approach could be adapted to our setting by avoiding the GANs and considering the mutual information between the mask and synthetic image and the original composite image as an additional objective.

A similar work by Zou et al. (2023), ILSGAN, introduced an information-theoretic regularization which maximizes the independence (minimizes an upper bound on mutual information (Cheng et al., 2020)) between (1) the visible foreground (i.e., foreground pixels where the mask values are ones) and invisible background (i.e., background pixels where the mask values are zeros), (2) invisible foreground (i.e., foreground pixels where the mask values are zeros) and visible background (i.e., background pixels where the mask values are zeros). Additional losses are added to encourage non-zero and binary masks. While this work addresses the issue of preventing degenerate solutions, a notable drawback is the utilization of multiple loss functions which requires a careful fine-tuning for the weight of each loss.

Chen et al. (2019) proposed ReDO as an unsupervised object segmentation method based on the assumption that foreground texture and background content are statistically independent (e.g., a flower can change color regardless of its background). Their model consists of a segmentation network that predicts a soft mask and a generator network that produces a new foreground texture conditioned on a Gaussian noise vector. The final output image is formed by alpha-blending the generated texture and the original image using the predicted mask. To avoid degenerate masks (e.g., all-zero or full-coverage), they introduce a mutual information objective: a separate network is trained to recover the original noise vector from the generated image, encouraging the mask to preserve informative regions relevant to texture generation.

Singh et al. (2019) proposed FineGAN, a hierarchical gan that (i) generates the background image by using a vanilla GAN that only focuses on the background patches obtained using off-the-shelf object detection models, (ii) generates the shape and texture hierarchically by imposing a parent-child relationship between the generated shape and texture, where a shape (i.e., the parent) can have many textures (i.e., the child). This is realized by conditioning the generated texture on the code used to generate the mask. Note that for

generating the shape, infoGAN loss where it maximizes the mutual information between the code and the generated image as there is no access to real images that has no textures.

The work by Sauer & Geiger (2021) introduced a Counterfactual Generative Network (CGN), leveraging the concept of learning Independent Mechanisms (IMs) to establish a causal structure for mask, foreground, and background. Each was modeled by fine-tuning a distinct pretrained BigGAN. To ensure the resulting composite image is real, they minimize the MSE loss between the output of pre-trained frozen BigGAN and the composition process. To ensure the generated mask is not trivial, hinge and entropy losses are deployed. For the background loss, the predicted saliency is minimized which leads to the foreground object's disappearance. For background generation a pre-trained U2Net is used to detect the saliency. Overall, this approach heavily relies on pretrained models and necessitates the incorporation of specific losses to prevent degenerate or trivial solutions.

He et al. (2022) proposed GANSeg, a generative model that synthesizes foregrounds, backgrounds, and segmentation masks in a hierarchical manner. Foreground and mask generation are conditioned on spatial embeddings derived from Gaussian noise, which encode part-specific locations. Each object is composed of multiple segments with each segment having its own mask; the final object mask is obtained by aggregating these individual masks. To avoid degenerate solutions where the masks collapse to all-zeros or all-ones, a hinge loss is applied to constrain the overall mask area. Additionally, a geometric consistency loss encourages each segment's mask to be spatially concentrated around its designated location, promoting more structured and interpretable mask generation.

The work by Li et al. (2023) proposes a training-free image segmentation method that leverages pretrained generative inpainting models, such as latent diffusion models (Rombach et al., 2022). Given an initial coarse mask (e.g., a bounding box), the image is first inpainted to hallucinate the background in place of the masked foreground. A contrast map is then computed by comparing the original and inpainted images, using both pixel-wise color differences and L-2 distances in the feature space of a pretrained encoder that preserves spatial resolution. K-means clustering (with $k = 2$) is applied to this contrast map, and the cluster with the higher mean contrast is interpreted as the refined foreground. This enhanced mask is then used in an outpainting step, in which the background is masked and reconstructed using the generative model. The contrast between the original image and this outpainted version is again analyzed to further refine the segmentation mask, following the same contrastive and clustering strategy. This process is iterated multiple times to resolve false positives and false negatives in the initial segmentation. While this method is notable for requiring no supervised training, its reliance on powerful pretrained generative models may limit its applicability in domains where such models are unavailable or underperforming. Moreover, its segmentation quality is contingent on the inpainting fidelity and the robustness of contrast-based clustering

To summarize, the presented works rely on either pretrained models or complex combinations of loss functions—involving training GANs, dependencies that our approach avoids.

### A.2 Vision-Transforms-based Models

The vision transformer (ViT) (Dosovitskiy et al., 2021) treats patches of input as tokens whose representations are processed through layers involving multi-head attention, and can be adapted to unsupervised segmentation. For example, the work by Wang et al. (2023b) used the ViT model DINO (Caron et al., 2021) to obtain features from non-overlapping patches of the input image. These features were used to construct a graph that represents the similarity between the patch-wise features. The normalized cut (N-cut) (Shi & Malik, 2000) algorithm was then applied, which was followed by CRF (Lafferty et al., 2001) for edge enhancement. A similar work was proposed by Wang et al. (2023a) which uses multiple N-cuts on masked images to detect multiple objects. Again, post-processing, such as conditional random field (CRF) (Lafferty et al., 2001) or bilateral solver (Barron & Poole, 2016), is required to get pixel-wise masks from the coarse patch-wise segmentation.

ViTs require large amounts of training data (Dosovitskiy et al., 2021), which can hinder the performance of the presented works if sufficient data is unavailable or if the data domain differs significantly from that of the pretrained ViT models. Even with sufficient data for ViT training, the demand for significant computational

resources remains, posing an additional constraint (Irandoust et al., 2022). All the works mentioned below depend on pretrained models, which is limiting for specialized image modalities.

The work by Hamilton et al. (2022) proposed an unsupervised semantic segmentation approach that distills knowledge from pretrained feature extractors. A frozen backbone (e.g., DINO-ViT) is used to extract dense pixel-wise features from input images. A trainable segmentation network maps these features to lower-dimensional embeddings representing per-pixel segment assignments. During training, a mini-batch is constructed for each sample by including its K-nearest neighbors in the feature space. The model then samples a neighbor image and computes a cosine similarity matrix between the pixel features of the target and the neighbor. The segmentation output is encouraged to be similar for pixels with high feature similarity and dissimilar for pixels with low similarity

### A.3 Class-Activation-Map-based Models

Much work on weakly-supervised segmentation is based on class-activation maps (CAM) derived from pretrained convolutional object classification networks Kumar Singh & Jae Lee (2017); Wei et al. (2017); Zhang et al. (2018); Li et al. (2018); Hou et al. (2018); Jiang et al. (2019). We stress the fact that our model does not require labeled data (for instance, class information for composite/background images). Performance was initially limited as segmentation based on activation maps often focused on a few parts of the objects (Kumar Singh & Jae Lee, 2017; Wei et al., 2017). To mitigate this problem, Zhang et al. (2018) used a backbone fully-convolutional network to extract initial CAMs and then used two parallel-branches, each a CNN classification network, which took the initial CAM as an input. Parts of the input CAM of the first classifier is erased with the guidance of the object localization map from the second classifier. This encourages the first classifier to seek other parts of the image to do the classification. Thus, this results in learning a more coherent/complete feature map that can be used for object segmentation. Similarly, Li et al. (2018) proposed two networks, where one network uses the parts that are neglected by the first one for the classification task which results in expanding the activation map to other related parts. The work by Hou et al. (2018) introduced an approach for adversarial learning during supervised classification training which encourages the CAM to expand from covering only part of the target objects while penalizing it for covering background regions spuriously using the background prior (i.e., regions with low activations defined as background, regions with high activations defined as foreground and regions in-between defined as potential foreground) obtained from the initial map Following a similar aim, Jiang et al. (2019) observed that the attention maps produced by a classification network changes focus on different object parts throughout the learning. They saved copies of the model each epoch and then used them to produce CAMs. At the end, they fused all the resulting CAMs using a pixel-wise max operation, which enhanced the final CAM. All the previously mentioned work in this paragraph depends on pretrained models.

The work by Chang et al. (2020) joined supervised learning with self-supervised learning to enhance CAM. First a CNN is trained to classify images according to their true labels. After that, the internal representation of the input image is used as a feature representation. The aggregated feature representations are then used to cluster each class into pseudo-labels (e.g., person label can be divided into child and adult). Then, another classifier is trained to classify the pseudo-labels/clusters of the feature representations while backpropagating the loss to fine-tune the original CNN to improve the feature representation. After that, the thresholded resulting CAM is used for semantic segmentation.

The work by Lee et al. (2021) uses information obtained from an off-the-shelf, pretrained saliency detector (trained in supervised or unsupervised fashion) to improve the CAM semantic segmentation. They minimize the loss between the estimated saliency map based on CAMs and the one obtained from off-the-shelf models while minimizing the classification loss.

Wu et al. (2021) initially extracted the class-specific CAMs obtained from an off-the-shelf model (i.e., for each input image, $K$ CAMs are generated where $K$ are the number of classes). Then, a self-attention mechanism is applied to all $B \times K$ CAMs , where $B$ is the batch size, from the batch, enabling the model to capture both spatial dependencies within each CAM (intra-CAM) and semantic relationships across different CAMs (inter-CAM), thereby improving attention consistency and completeness. The output then used to classify

the input image based on its multi-label obtained by the $K$ activation maps. During inference, the activation maps obtained from the self-attention model are used for semantic segmentation.

The work by Xu et al. (2022) proposed a multiclass transformer that learns class tokens in a classification setting. The basic idea is to learn the interaction between the patches and different class tokens and use the resulting similarity to refine the resulting activation maps from the transformer, which is later used for semantic segmentation. The training loss comprises two multi-label soft margin losses. One is based on the class tokens and the other is based on patch tokens. These losses are calculated between the ground-truth labels at the image level and the predictions for each class. Their implementation depends on a pretrained model on ImageNet and they used multi-scale testing (i.e., processing the same input image at different scales and then combining the results) and CRFs for post-processing.

The work by Xie et al. (2022) introduced a class-agnostic contrastive learning framework for semantic segmentation (C2AM) with pretrained models as backbone for features extraction. Using a pretrained model activation maps for extracting background and foreground features, a contrastive learning approach is used to separate foreground and background by encouraging the similarity within each foreground and background representation and dissimilarity across foreground and background representations. The foreground and background representations are separated by a matrix multiplication with a thresholded mask based on the value of the activations. The mask is obtained by the pretrained model's activation maps.

Overall, the work presented in this section relies on pretrained models, typically trained on large datasets. We demonstrate that training models from scratch on synthetic data does not yield useful CAMs, which are crucial for achieving high performance in this line of work.

### A.4 Other Work

Hung et al. (2019) proposed SCOPS, a self-supervised part segmentation framework that leveraged multiple auxiliary objectives. First, they used saliency maps extracted from a pre-trained classification network as soft supervision, encouraging the encoder's part activation maps to align with semantically meaningful regions via a cosine similarity loss. Second, they introduced a geometric loss that encouraged all pixels assigned to a given part to be spatially concentrated around that part's center; the number of parts was treated as a hyperparameter. Lastly, an equivariance loss ensured that part assignments remained consistent under random spatial transformations such as rotation and scaling, promoting robustness and part consistency.

The work by Savarese et al. (2021) proposed an unsupervised model-free method to segment foreground and background based on minimizing the mutual information between the segmented foreground and background. They used a variant of information theory, namely the coefficient of constraint that prevents trivial solution including an entropy in the denominator. By including assumptions about the conditional distributions (i.e., Laplace distribution for foreground/background given background/foreground), the loss is equivalent to maximizing the inpainting errors of both the masked foreground and the masked background. However, they added a new loss that penalizes the texture diversity within the masked region (i.e., the masked region should have a uniform texture)

## B Statistical Divergences

In this section, we review statistical divergences, particularly the sliced Wasserstein distance, which serves as the backbone loss for our approach, as explained in the next section.

Previous work in unsupervised foreground object masking (see Section 2) has relied on discriminator networks and adversarial loss functions as in the original GAN (Goodfellow et al., 2014), which exploit the fact that the cross-entropy loss of the ideal discriminator is proportional to the Jensen-Shannon divergence. Since Goodfellow et al. (2014)'s seminal work, a variety of statistical divergences have been used to train GANs, namely $f$-divergences (Nowozin et al., 2016) and maximum mean discrepancy (MMD) (Li et al., 2017).

The family of Wasserstein distances is another class of divergences based on optimal transport theory (Villani et al., 2008). In particular, the Wasserstein-1 distance, a statistical divergence also known as the Earth mover's distance, has been applied in generative modeling in the form of the Kantorovich dual (Arjovsky

et al., 2017). Note that all of these divergences require adversarial optimization (MMD-GAN (Li et al., 2017) uses adversarial selection of the kernel). In contrast, the primal form of the Wasserstein-$p$ distance measures the divergence between the distributions of two random variables $X \sim \mathbb{P}_X$ and $Y \sim \mathbb{P}_Y$ in terms of the optimal transport plan

$$\mathrm{W}_p(\mathbb{P}_X, \mathbb{P}_Y) \triangleq \left( \inf_{\mathbb{P}_{XY} \in \mathcal{P}_{\mathbb{P}_X, \mathbb{P}_Y}} \mathbb{E}_{(X,Y)\sim \mathbb{P}_{XY}} d(X,Y)^p \right)^{\frac{1}{p}}, \tag{10}$$

where $\mathcal{P}_{\mathbb{P}_X, \mathbb{P}_Y}$ defines the set of transport plans, consisting of all joint distributions with marginals equal to the original distributions $\mathbb{P}_X$ and $\mathbb{P}_Y$, and $d$ is a distance function. For $X, Y \in \mathbb{R}^d$, the Euclidean distance is typically used $d(X,Y) = \|X - Y\|_2$.

In practice, only samples are available, and for training divergence estimates require computation on batches. For batches of size $N$, the computational complexity of variational approaches (Nowozin et al., 2016; Arjovsky et al., 2017) is $\mathcal{O}(N)$, compared to $\mathcal{O}(N^2)$ for MMD (Li et al., 2017), and $\mathcal{O}(N^3)$ for the primal form of Wasserstein-$p$ distance. To mitigate the computational bottleneck of the Wasserstein distance for samples, the Sinkhorn algorithm has been applied to solve an entropically regularized version of equation 10 (Cuturi, 2013). Another alternative, is to exploit the sliced Wasserstein distance (Kolouri et al., 2018), as the one-dimensional case of Wasserstein-$p$ distance requires only $\mathcal{O}(N \log N)$, due to a closed form (Santambrogio, 2015) that requires sorting. The sliced Wasserstein (SW) distance is motivated by the Cramér-Wold theorem (Bélisle et al., 1997), which states that probability measures in Euclidean space are characterized by all one-dimensional projections, which corresponds to the integration of the Wasserstein distance across all one-dimensional slices (Wu et al., 2019; Deshpande et al., 2018; Kolouri et al., 2018). In practice, this integration is an expectation that can be computed by Monte Carlo integration by sampling from a uniform distribution over the unit hypersphere $\mathbb{S}^{d-1}$.

$$\begin{aligned} \overline{\mathrm{SW}}_p^p(\mathbb{P}_X, \mathbb{P}_Y) &\triangleq \int_{\mathbb{S}^{d-1}} \mathrm{SW}_p^p(\mathbb{P}_X, \mathbb{P}_Y; w)\, dw \\ &= \mathbb{E}_{W \sim U(\mathbb{S}^{d-1})} \left[ \mathrm{SW}_p^p(\mathbb{P}_X, \mathbb{P}_Y; W) \right], \\ \mathrm{SW}_p(\mathbb{P}_X, \mathbb{P}_Y; w) &\triangleq \mathrm{W}_p(\mathbb{P}_{w^\top X}, \mathbb{P}_{w^\top Y}). \end{aligned} \tag{11}$$

Given two samples/batches $\hat{\mathbb{P}}_X = \{(\frac{1}{N}, \mathbf{x}_i)\}_{i=1}^N$ and $\hat{\mathbb{P}}_Y = \{(\frac{1}{N}, \mathbf{y}_i)\}_{i=1}^N$, the computation of the sliced Wasserstein-$p$ distance is simply the mean of the absolute error to the $p$th power between paired samples after sorting: $\widehat{\mathrm{SW}_p^p(\mathbb{P}_X}, \hat{\mathbb{P}}_Y; \mathbf{w}) = \frac{1}{N} \sum_{j=1}^N (\mathbf{w}^\top \mathbf{x}_{\pi_j} - \mathbf{w}^\top \mathbf{y}_{\sigma_j})^p$, where the permutations $\pi$ and $\sigma$ ensure that $\mathbf{w}^\top \mathbf{x}_{\pi_1} \leq \mathbf{w}^\top \mathbf{x}_{\pi_2} \leq \cdots \leq \mathbf{w}^\top \mathbf{x}_{\pi_N}$ and $\mathbf{w}^\top \mathbf{y}_{\sigma_1} \leq \mathbf{w}^\top \mathbf{y}_{\sigma_2} \leq \cdots \leq \mathbf{w}^\top \mathbf{y}_{\sigma_N}$, respectively. Intuitively, $\mathbf{w}$ defines a subspace and the sorting ensures the shortest distances between the pairs in the subspace.

Alternatively, once can use energy-based Wasserstein (EBSW) (Nguyen & Ho, 2023) that depends on importance sampling to emphasize slices that distinguish the distributions:

$$\mathrm{EBSW}_p(\mathbb{P}_X, \mathbb{P}_Y; f) = \left( \mathbb{E}_{W \sim \sigma_{X,Y}(W; f, p)} \left[ \mathrm{SW}_p^p(\mathbb{P}_X, \mathbb{P}_Y; W) \right] \right)^{\frac{1}{p}}. \tag{12}$$

With a uniform proposal distribution over the hypersphere,

$$\sigma_{X,Y}(w; f, p) \triangleq \frac{f(\mathrm{SW}_p^p(\mathbb{P}_X, \mathbb{P}_Y; w))}{\int_{\mathbb{S}^{d-1}} f(\mathrm{SW}_p^p(\mathbb{P}_X, \mathbb{P}_Y; w'))dw'}, \tag{13}$$

where $f$ is a monotonic function. Importantly, this avoids an explicit search for the best slice (Deshpande et al., 2019). Using Monte Carlo integration, a set of $L$ random unit vectors $w_1, \ldots, w_L$ are drawn, importance sampling estimate approximate

$$\mathrm{EBSW}_p^p(\mathbb{P}_X, \mathbb{P}_Y; f) \approx \sum_{l=1}^L \frac{f(\mathrm{SW}_p^p(\mathbb{P}_X, \mathbb{P}_Y; w_l))}{\sum_{l'=1}^L f(\mathrm{SW}_p^p(\mathbb{P}_X, \mathbb{P}_Y; w_l'))} \mathrm{SW}_p^p(\mathbb{P}_X, \mathbb{P}_Y; w_l). \tag{14}$$

Interestingly, an analogous approach can be used to select from a predefined set of kernel functions for MMD (Biggs et al., 2023), which is provides a rough approximation of the adversarial optimization of the kernel function in MMD-GAN (Li et al., 2017).

# C Synthetic Datasets

## C.1 Synthetic Data Description

### C.1.1 Synthetic-Aperture Sonar Backgrounds with dSprites

This synthetic dataset is derived from real-world background-only synthetic-aperture sonar (SAS) images (Cobb & Zare, 2014), augmented by overlaying artificial objects to simulate relevant scenarios. This SAS dataset contains 129 $1001 \times 1001$ images that are originally complex-valued, single (high-frequency) channel, taken from various seafloor texture types. For each sonar scene, we crop 200 $64 \times 64$ images from the magnitude images. We normalize each crop by its mean and then clip any value larger than 16. Half of the resulting crops are used as composite images where we paste objects from dSprites (Matthey et al., 2017) dataset using equation 1. The data is divided into $70\%, 20\%,$ and $10\%$ for training, validation, and testing.

We select the dSprites dataset because the shapes resemble real man-made objects observed in sonar images. However, since the dSprites shapes lack intensity variations, we introduced a smooth gradient to each dSprite object, which mimics the consistent intensity patterns typical in SAS imaging systems. This gradient follows a planar transition with a 45-degree slope and is applied based on the corresponding crop values. The minimum value of the transition is chosen randomly between the 50th and 70th percentiles of the crop values, while the maximum value is randomly selected between the 80th and 100th percentiles of the crop values. This dependence on the background intensity values makes the foreground object brighter in a bright crop and dimmer in a dim one. This makes the segmentation task more challenging since using a simple threshold will not produce a reasonable mask. We use the other half as background images.

### C.1.2 Textures with MNIST, FashionMNIST, and dSprites

This synthetic dataset consists of surrogate data, represented as grayscale single-channel images, which we use to further demonstrate and validate the method's functionality. We sourced background images from crops of 10 different textures obtained from the Brodatz dataset (Brodatz, 1966). For foreground objects, we used MNIST, Fashion MNIST (Xiao et al., 2017), and dSprites (Matthey et al., 2017). These datasets reflect a variety of foreground objects: MNIST are medium extent, thin objects with high pixel values; Fashion MNIST are objects of large extent, a diversity of shapes, some almost-convex, and varying in pixel intensities; and dSprites are small compact shapes (we created an artificial range of intensity values).

For the synthetic dataset, $140,000$ background images of size $64 \times 64$ were generated by randomly patching the texture images. Half of the background images were used as background for the composite images. This resulted in $70,000$ images as foreground and background. Images in the foreground datasets were resized to $64 \times 64$ and the true (binary) mask was used to blend it onto the background image using equation 1. Since MNIST and Fashion MNIST have no given true mask, we estimate the true mask by applying Otsu's threshold on each image (Otsu, 1979). The data is divided into $70\%, 20\%,$ and $10\%$ for training, validation, and testing.

Again, since the dSprites images lack intensity variation, we create random intensities for each foreground object pixel by sampling a Gaussian distribution with zero mean and unit standard deviation and then squaring it to remove negative values. We then min-max normalize the resulting composite image such that the lowest intensity value is 150 and the max is 255, before masking a background and combining the two. Each image is min-max normalized such that all pixel values are between $[0, 1]$.

## C.2 Implementation Results

We note here any dataset dependent implementation details.

For SAS+dSprites and Textures+MNIST/FashionMNIST/dSprites, the surrogate data cluster labels for the composite images are computed by processing the corresponding background-only images through both the AE/CLE and Sinkhorn K-means. For the SAS images, we find that AE architecture is not able to reconstruct the images, so we use a symmetrical architecture that is composed of four blocks for the encoder and decoder,

and each block is composed of convolution, ReLU, BatchNorm, with residual units: the 64-channel block has 1 and other blocks have 2 residual units each. The number of channels per block is $\{64, 128, 256, 512\}$, with an additional 768-channel stage. As described above, a fully connected bottleneck layer of dimension $o = 20$ is used to represent the latent space.

The Textures+MNIST/FashionMNIST/dSprites images, have 10 ground truth clusters and we experiment with varying the number of clusters, choosing values from the set $\{5, 10, 15\}$

For SAS images, we choose cluster values from the set $\{3, 4, 5\}$. Initial experiments with 2 clusters consistently failed to separate visually distinct regions.

For Textures+MNIST/FashionMNIST/dSprites and SAS+dSprites datasets, we run the training for 50 and 100 epochs, respectively. For the former, we choose the model with lowest validation loss $\mathcal{L}$ shown in equation 8, but for the latter we also include a quantile loss equation 15 with quantile, $q = 0.8$, such that the maximum area of an object is 20% of the image size:

$$\mathcal{L}_{\text{quantile}}(\theta) = \mathbb{E}_{X,R}\left[\sum_{ij\in\mathcal{Q}} \left([\tilde{X}_\theta]_{ij} - R_{ij}\right)^2\right], \quad \mathcal{Q} \quad = \{ij : M_\theta(X)_{ij} \leq \tau\}, \quad \tau = \text{quantile}\left(M_\theta(X), q\right). \quad (15)$$

That is, for the SAS+dSprites dataset the total loss is $\mathcal{L}_D(\theta) + \mathcal{L}_{Bg}(\theta) + \mathcal{L}_{\text{quantile}}(\theta)$. This additional loss encourages the masking network to produce counterfactual images in which a $q$th fraction of its pixels match the source background, essentially encouraging the corresponding mask pixels to be zero.

### C.3 Results: MNIST, FasionMNIST, and dSprites on Textures

We provide both quantitative and qualitative results for three datasets: MNIST, Fashion MNIST, and dSprites. Initially, we trained the segmentation model using true clusters, defined by the texture label. Subsequently, we trained the segmentation model based on AE clustering. We begin by presenting quantitative results, followed by showcasing qualitative outcomes for the best-performing models on each dataset.

Figure 5 shows the average precision, AUCROC, and mean IOC values for different numbers of clusters. The best performance appears to be at 5 clusters, where the average precision is 43%, AUC-ROC value is 78%, and 30% mean IOC. On the other hand, high number of clusters seem to not encouraging better performance.

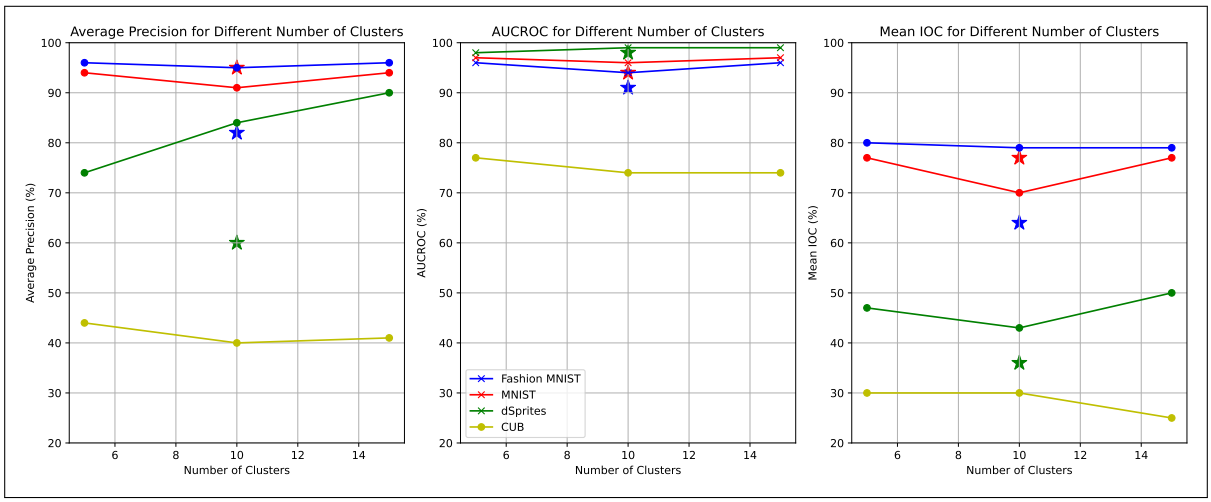


Figure 5: The percentage of Average Precision, AUCROC, mean IOC values (y-axis) for the four datasets, as indicated by the legend. The x-axis represents the chosen number of clusters for the K-means model based on AE/CLE features. The star symbols above the x-axis values, specifically at the position of 10, emphasize the Average Precision and AUCROC corresponding to the ground truth clusters.

We show 8 testing images, the estimated masks, the true masks, and the thresholded estimated mask based on 0.5 in Figure 6. We refer to the evaluation values corresponding to the model trained using the true clusters by the ground truth values. Figure 5 shows the results for the three datasets with respect to the number of clusters from K-means. The star shows the performance using the ground truth values (i.e., the true texture class).

The performance of the model on Fashion MNIST is high with all clusters performing relatively the same. The Fashion MNIST objects are relatively large with polygonal-like shapes and the masks are accurate as shown in Figure 6.

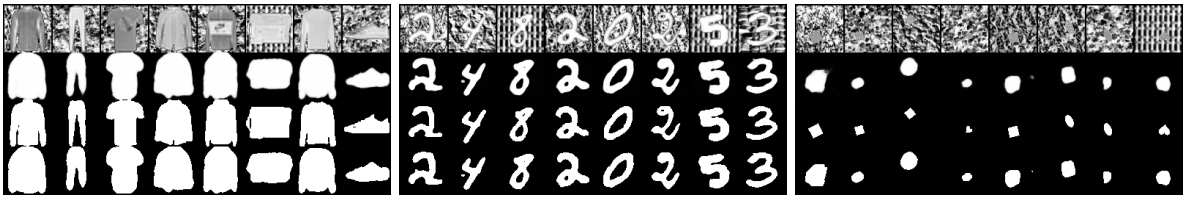

Figure 6: Results of the segmentation model for Fashion MNIST (left), MNIST (middle), and dSprites (right). From top to bottom: input images, estimated masks, true masks, and thresholded estimated masks at .5

The model performs similarly on MNIST when utilizing any synthetic clusters, except for a slight drop when using the 10 clusters. We notice, however, that the performance of the true clusters is worse compared to the synthetic one. As shown in Figure 5, the performance drops when using true clusters.

The model's performance on the dSprites dataset is comparatively lower, which we primarily attribute to the small size of objects and intensity variation. Despite this, the qualitative results depicted in Figure 6, show that as in the case of sonar data, the masks are not 'sharp'. It is noteworthy that the mask size is proportional to the object size. Notably, when employing AE-based clustering with a cluster number equal to 10, the dataset achieves the highest average precision at 83%, compared to 60% when using true clusters.

To further discuss the reason for the superior performance for synthetic clusters, we show the clustered background using AE-K-means along with the corresponding true clusters in Figure 7. We notice that the K-means clustering creates clusters out of the same true cluster, and each cluster has a different phase. For example, in the case of 5 clusters, the brick cluster is divided into two out-of-phase clusters. It also groups together distinct true backgrounds into one cluster. For example, in the case of 5 clusters, the first row, which represents a cluster, shows a mix of two true clusters. The sliced Wasserstein distance is insensitive to out-of-phase differences, making it difficult to quantify these differences. Consequently, images with identical content but differing phase are challenging to assign to the same distribution.

Finally, we show the performance of the masking network when using true clusters in Figure 8.

#### C.3.1 Unsupervised Object Segmentation Benchmarks

For the synthetic datasets, since we have more class information about the background and objects, we can train a classification model and use its resulting CAM. We use the method introduced by Xie et al. (2022) as a benchmark as it gives the best results among the CAM-based models. We find it one of the closest methods to our work due to its weakly supervised nature. We also use the GAN-based method, PerturbGAN, introduced by Bielski & Favaro (2019). Both of them fail to converge to a meaningful object masks when using synthetic single-channel data. In order to compare the performance of the related work using our synthetic data, we train PerturbGAN (Bielski & Favaro, 2019) on our composite images (excluding background images). We also found that the work by Xie et al. (2022) (C2AM) can be adapted to take advantage of the composite and background images. Thus, we train a ResNeT-52 model (their backbone model) to classify the composite images based on their foreground objects class, and to classify background images based on their texture label. We choose this classification task to encourage the ResNeT model to learn a rich representation that has enough entropy to be used as CAM. After training the backbone model, we proceed to fine-tune the model using their approach.

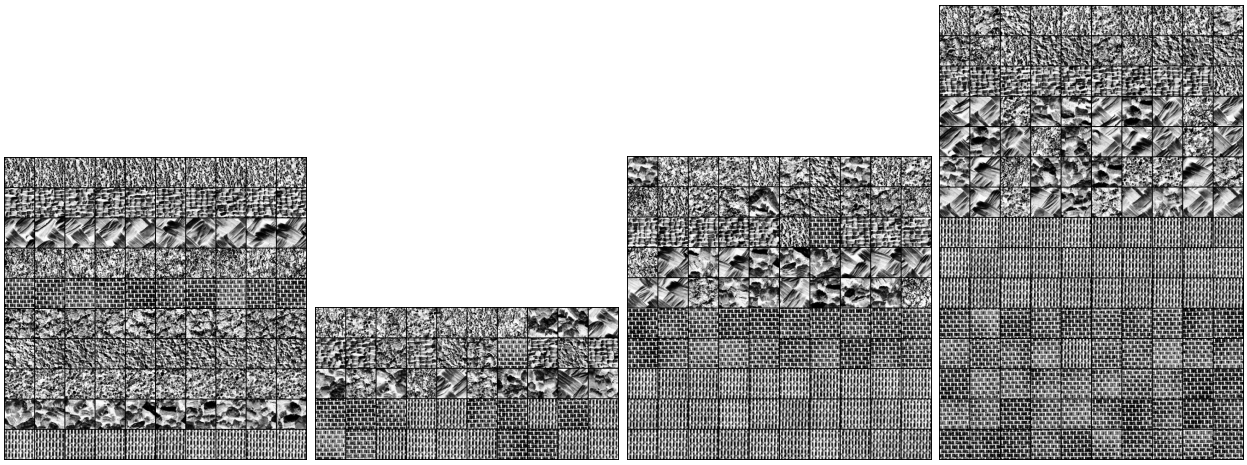

Figure 7: Background Clusters: From left to right: True clusters, 5, 10, and 15 clusters.

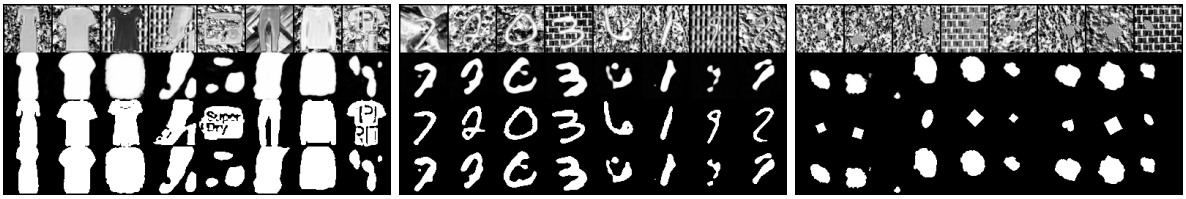

Figure 8: Results of the segmentation model for Fashion MNIST (left), MNIST (middle), and dSprites (right) using true clusters. From top to bottom: input images, estimated masks, true masks, and thresholded estimated masks at .5

We have noticed that PerturbGAN is able to generate similar images to the synthetic dataset; however, it was able to 'cheat' as the generated foreground mask did not represent the true foreground masks. Also, the generated background images have composite images and background images as shown in Figure 10.

For C2AM model (Xie et al., 2022), we notice that it failed to converge to a meaningful solution as shown in Figure 9. Note that these are training samples. We hypothesize this is due to a not well-trained backbone model; the model either needs more data or a more complicated modeling scheme, for which the two scenarios invalidate the minimalist approach that our method promotes.

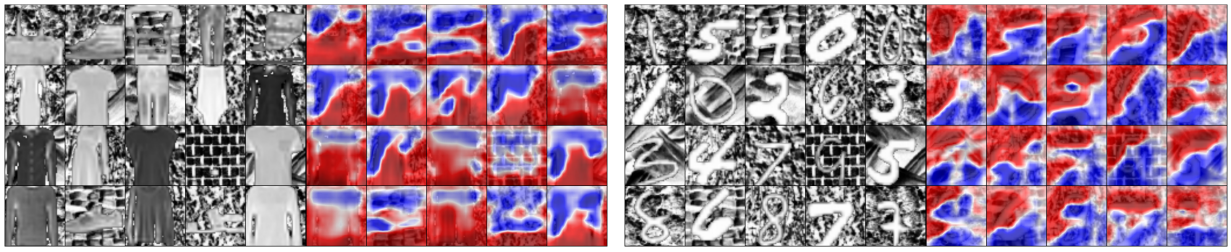

Figure 9: Results from C2AM model based on Fashion MNIST (left) and MNIST (right) datasets. Left of each block: the training input image. Right of each block: the activation maps where red shows the predicted foreground object.

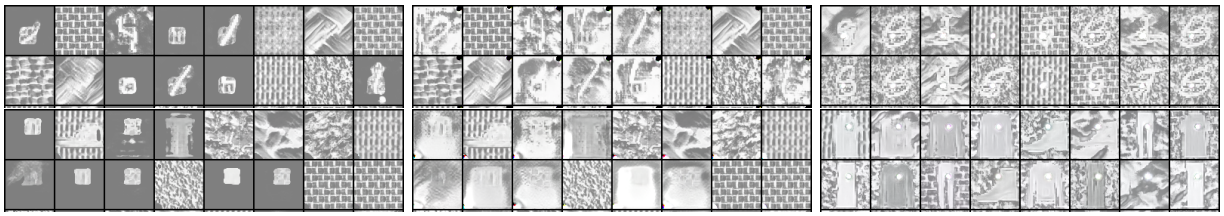

Figure 10: Results from PerturbGAN images based on MNIST (top) and Fashion MNIST (bottom) datasets. From left to right: generated mask along with the generated composite images, generated composite images, and generated background images.

### C.4 Results: Synthetic Object on Real Sonar Dataset

We present both quantitative and qualitative results for the sonar dataset that combines real-world seafloor imagery from Cobb & Zare (2014) with synthetic objects from the dSprites dataset. The seafloor contains six texture categories: sand ripple, rock, coral, sand, mud, and seagrass.

Figure 11 illustrates the segmentation performance, demonstrating that the proposed method generates high-quality segmentation masks. However, for this dataset, the method does not produce 'sharp' masks.

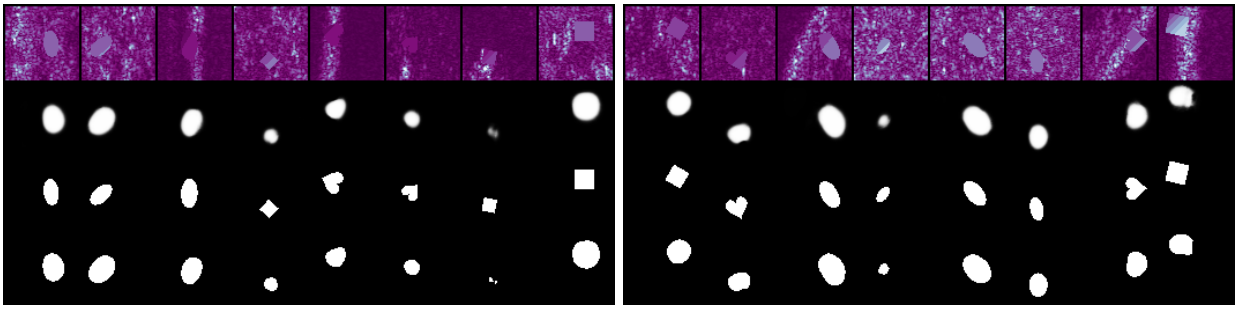

Figure 11: Results of the segmentation model for sonar images. From top to bottom: input images, estimated masks, true masks, and thresholded estimated masks at .5.

Table 5 provides the performance metric values for different numbers of background clusters. The results indicate that the best performance is achieved when using four clusters.

Table 5: Performance Metrics Across Different Number of Clusters for Sonar Data

| Clusters | Avg. Precision (%) | Mean IoC (%) | AUC-ROC (%) |
|---|---|---|---|
| 3 | 60 | 30 | 90 |
| 4 | 82 | 57 | 97 |
| 5 | 22 | 20 | 87 |

## D Additional Results

### D.1 SSS Dataset

Figure 12 shows cases where the masking network also includes shadows of ships.

In contrast, Figure 13 shows cases where the masking network is successful with less extensive shadows.

Figure 14 shows images without ships, where the model identifies the artificial reef, although it not in the ground truth. As a man-made object and arrangement it could be argued that the masking network worked

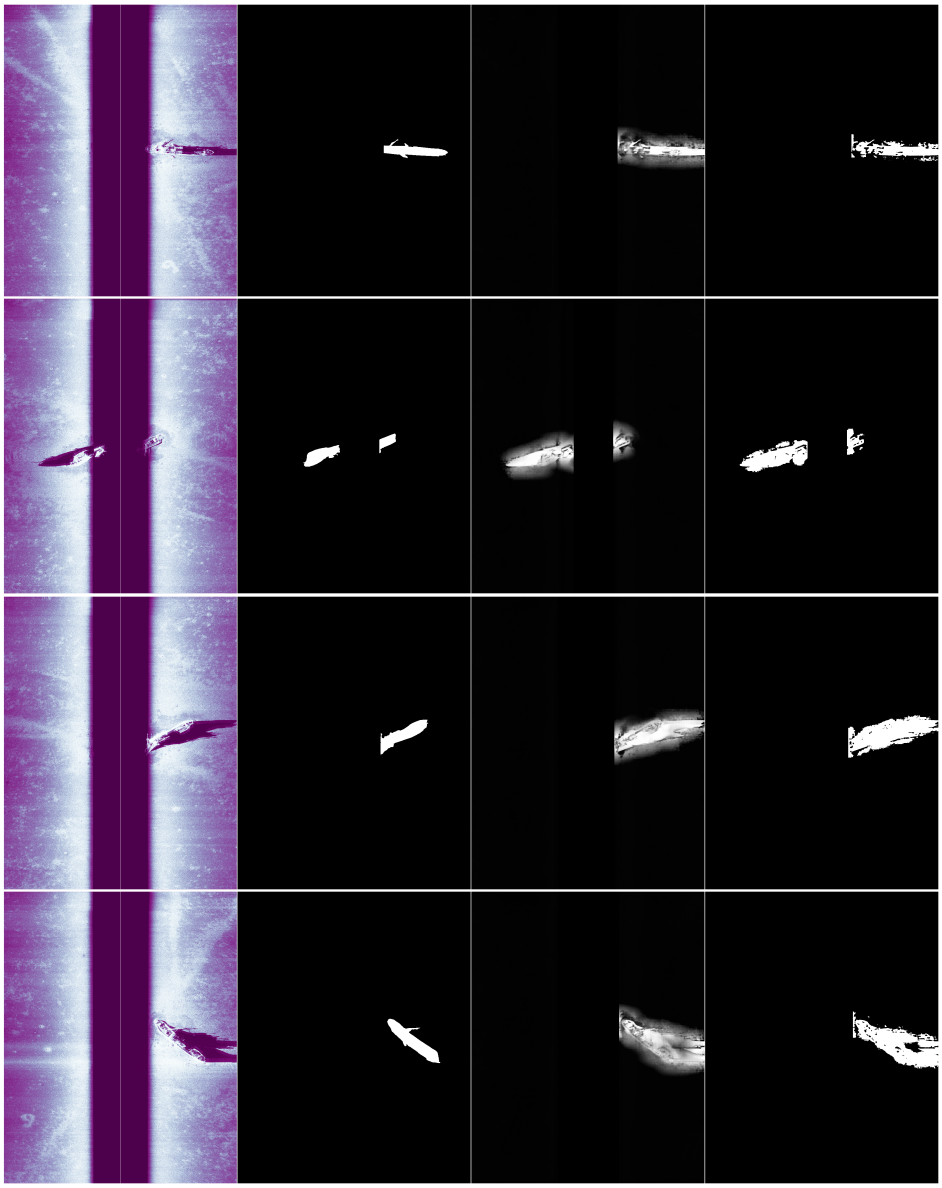

Figure 12: Segmentation model results on SSS images. Each row corresponds to a different image. From left to right: input images, ground truth masks, estimated masks, and thresholded estimated masks at 0.5. Image sites: Viator.

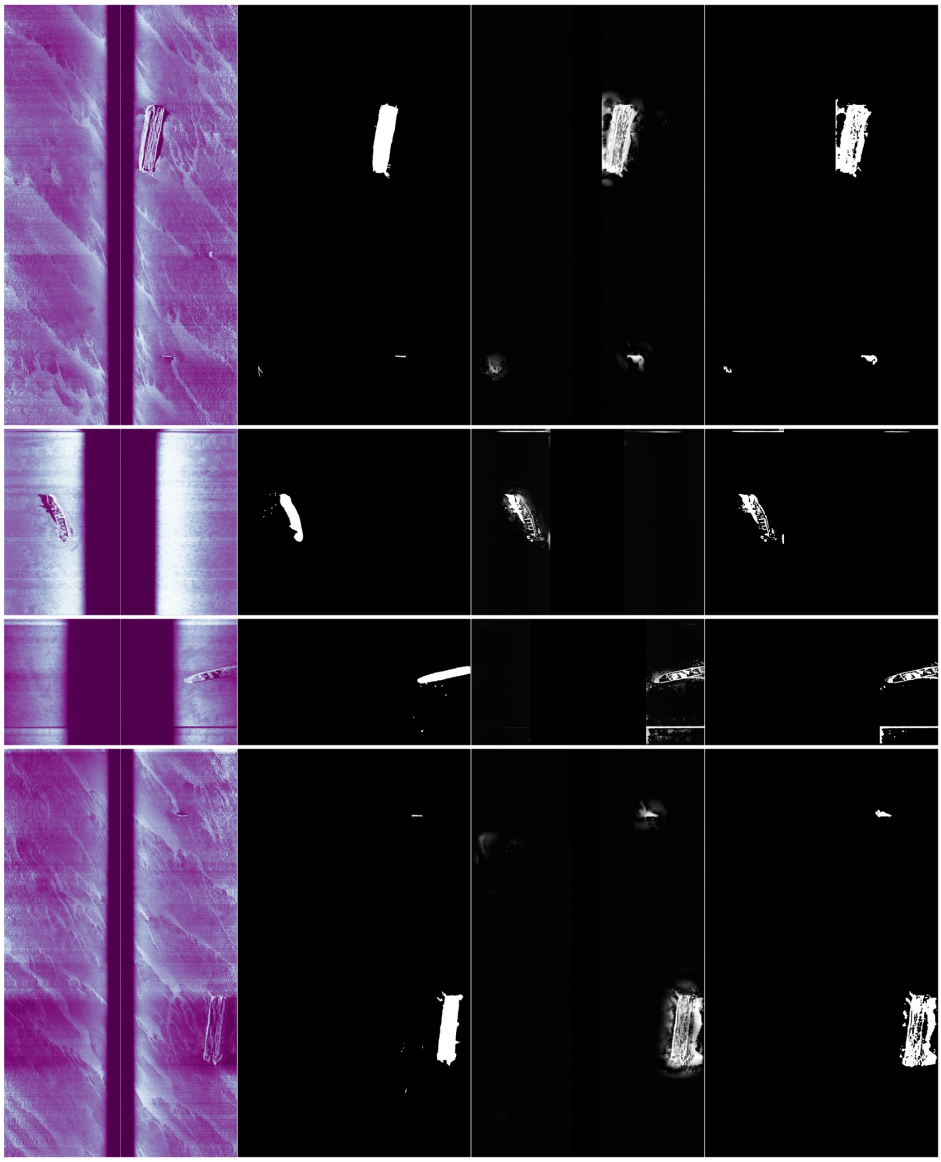

Figure 13: Segmentation model results on SSS images. Each row corresponds to a different image. From left to right: input images, ground truth masks, estimated masks, and thresholded estimated masks at 0.5. Images sites from top to bottom: Barge, WH Gilbert , WH Gilbert, and Barge.

in this case. However, it also highlights an image where there are extensive false positives for portions of the seafloor.

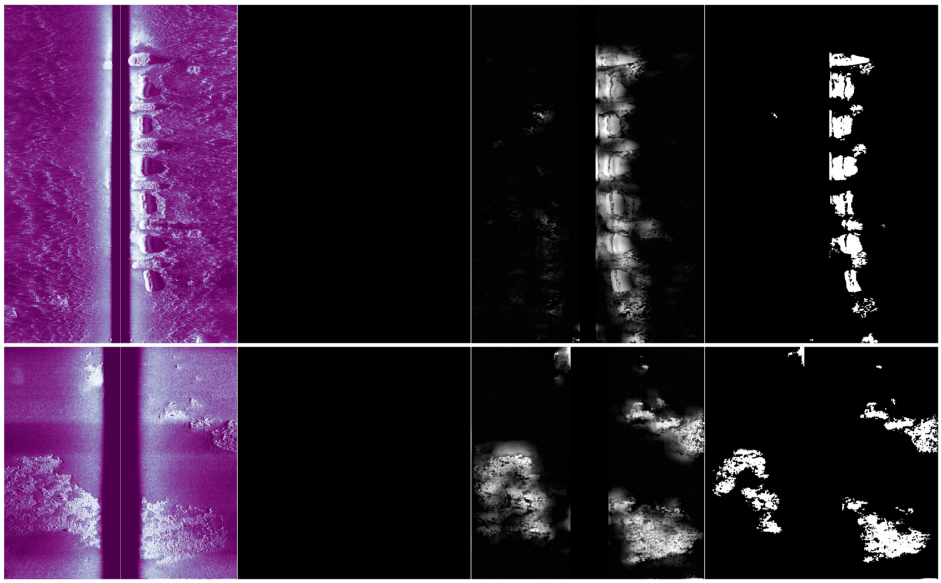

Figure 14: Segmentation model results on SSS images without ships, but regular arrangement of rocks or blocks in the first image. Each row corresponds to a different image. From left to right: input images, ground truth masks, estimated masks, and thresholded estimated masks at 0.5. Site of the first image is Artificial Reef, and for the second image is Haltiner Berge.

Figure 15 is another case with many false positives, that other supervised models also perform poorly on.

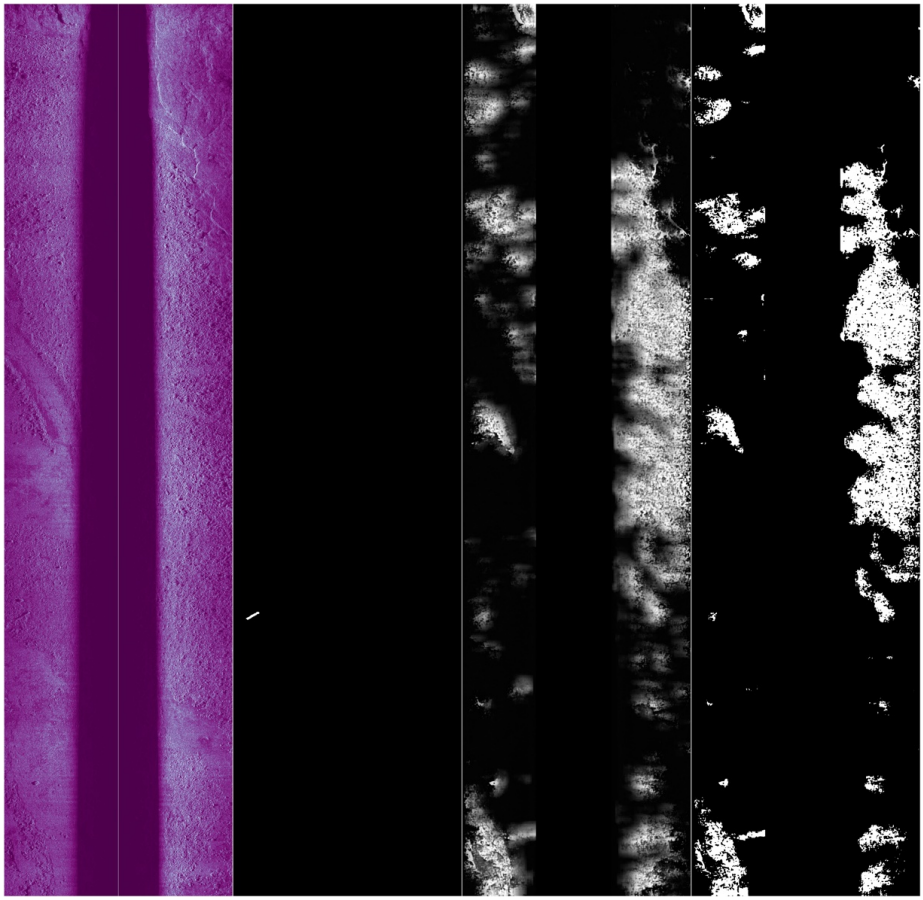

Figure 15: Failure cases of the segmentation model on SSS images at 'James Davidson'. From left to right: input image, ground truth mask, estimated mask, and thresholded estimated mask at 0.5.

### D.2 Benchmark Results

Attempts to apply unsupervised segmentation methods to the SSS dataset are shown in Figures 16, 17, 18, and 19.

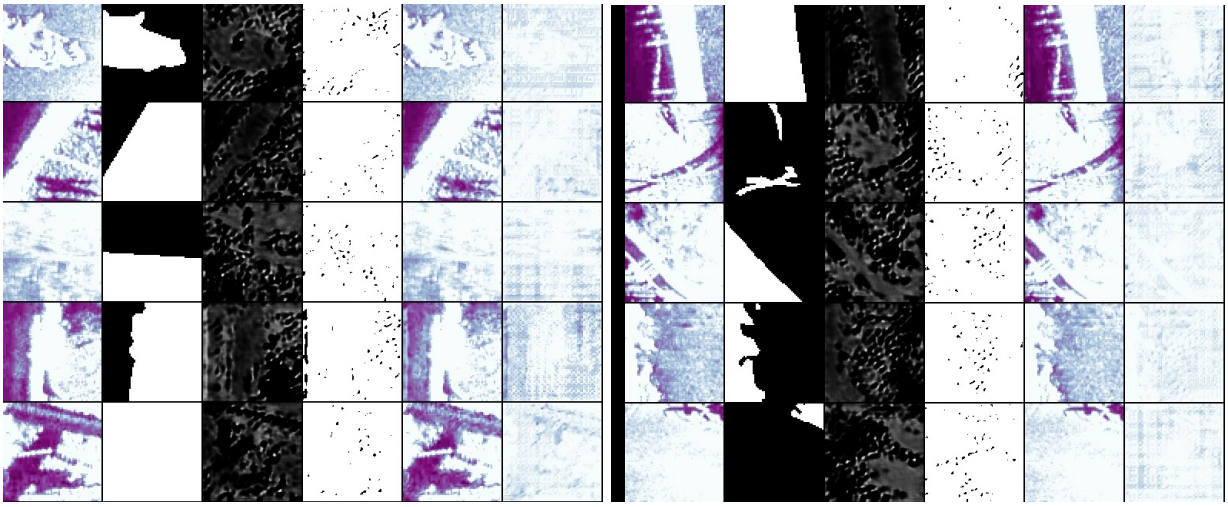

Figure 16: Two blocks of results from Chen et al. (2019) model on the SSS dataset. Each row represents the result of an input sonar patch: first column is the input sonar patch, second is the segmentation ground truth, third and fourth are generated masks, and the last two are alpha blended results based on the generated masks.

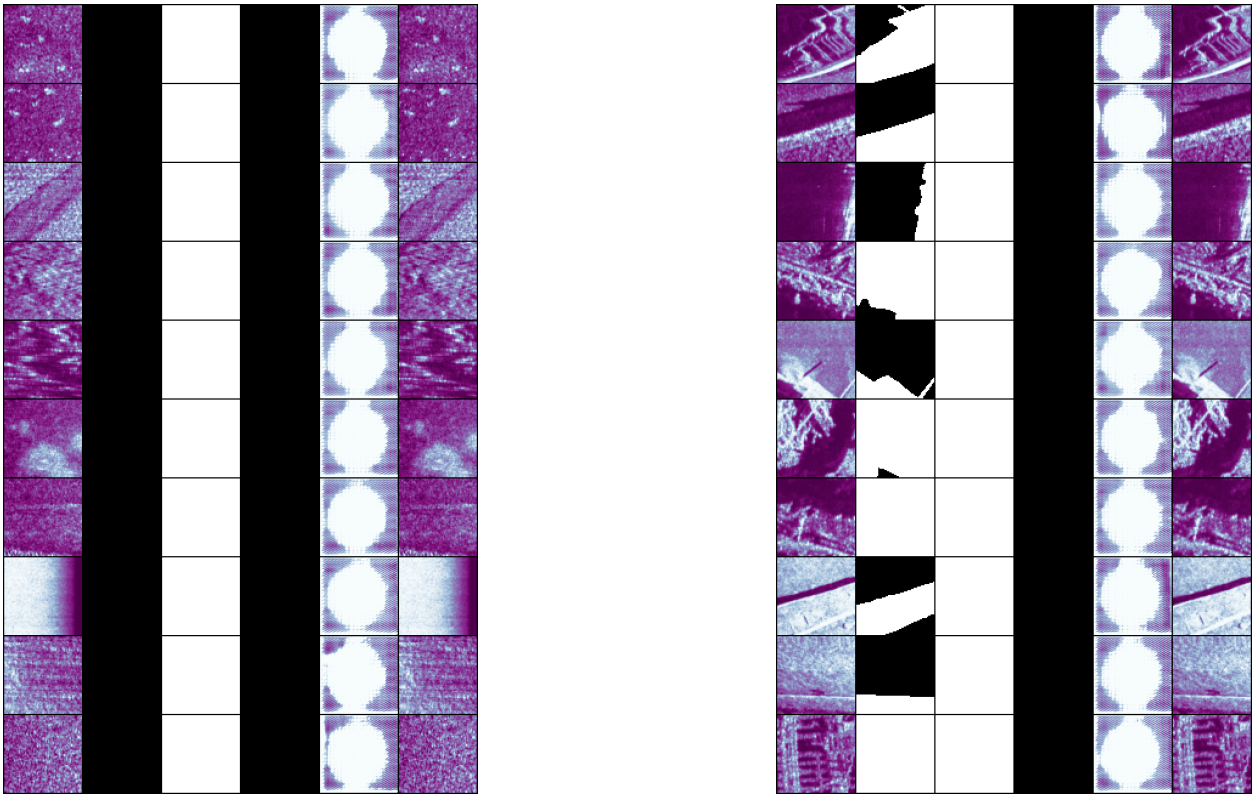

Figure 17: Two blocks of results from Chen et al. (2019) model on the SSS dataset. Each row represents the result of an input sonar patch: first column is the input sonar patch, second is the segmentation ground truth, third and fourth are generated masks, and the last two are alpha blended results based on the generated masks. The left figure shows a group of background patches and the right one shows a group of composite images.

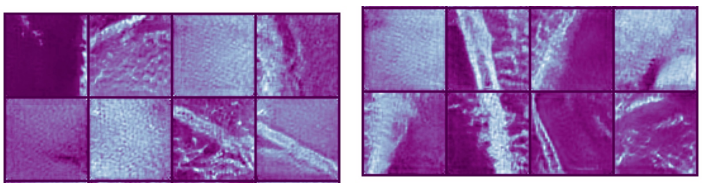

Figure 18: Generated images from ILSGAN (Zou et al., 2023) on the SSS dataset. Each cell represents a generated image.

.

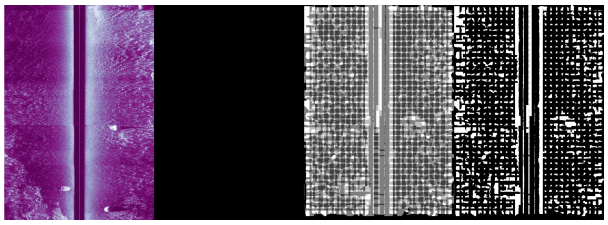

Figure 19: Results from model-free unsupervised baseline method Savarese et al. (2021) using patches with 50% overlaps on the SSS dataset.

### D.3 Additional Results for CUB Dataset

Additional counterfactuals from the model trained on the original CUB split are shown in Figure 20.

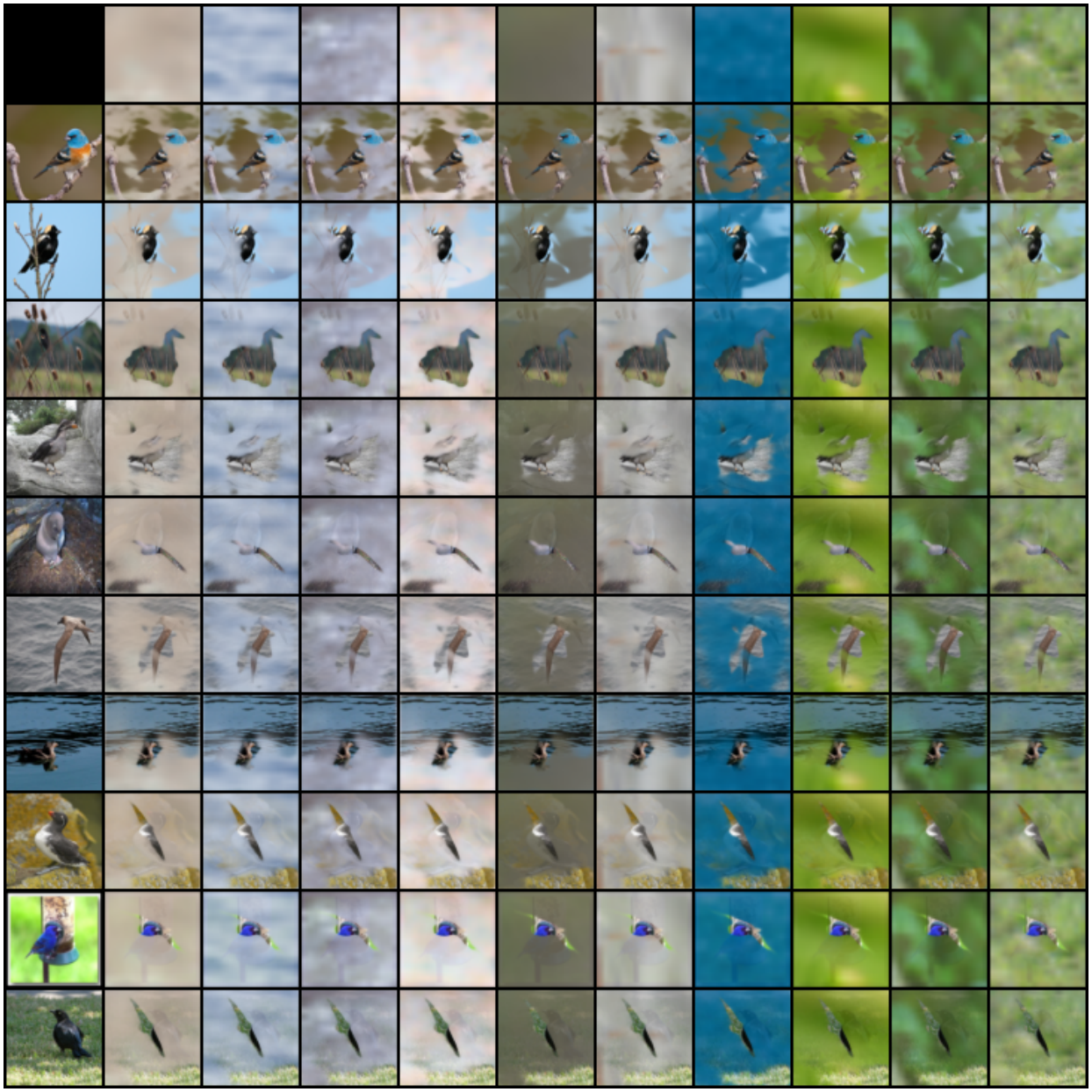

Figure 20: Generated counterfactual images based on test images using 10 clusters. The first row shows the source background image where each image comes from a different background cluster, and the first column is the source composite image. Each cell in the grid (except the first row and column) represents the alpha-blending of the corresponding source background and source composite images. Each column in this figure shows a background that corresponds to the source background at the top, and every row shows a foreground object that corresponds to the source foreground object at the most left, which demonstrates, generally speaking, that our method is preserving both background and foreground information. Also, the general appearance of the counterfactual images do correspond to the original data. It is interesting to see that in the last three rows, the model is able to craft counterfactuals with bird-like images that are not strongly related to the input composite images.

Figure 21 shows examples of the background images extracted from original CUB split organized into 10 clusters. Note that color and color are very distinct.

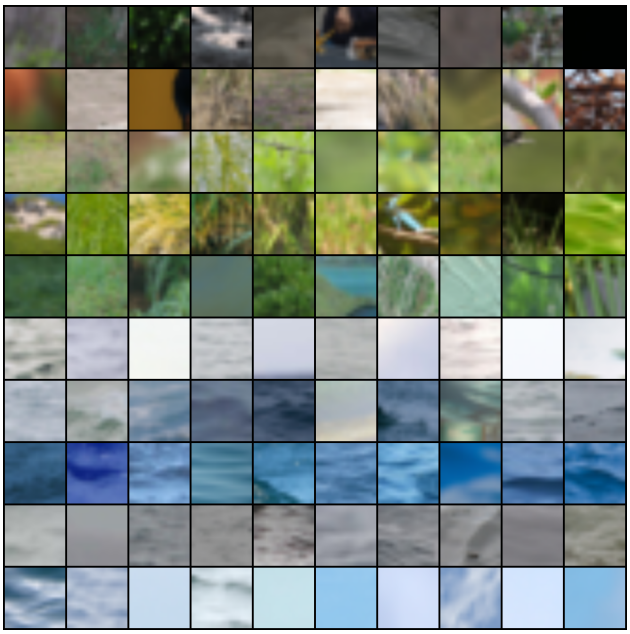

Figure 21: Each row shows an example obtained from clusters for the CUB dataset.

Sensitivity study of performance metrics for the choice of latent representation (auto-encoder or contrastive learning) and the number of clusters for the original CUB split are shown in Table 6.

Table 6: Masking Network Performance (mean IoC) Comparison of AE+K-means and CL+K-Means based Background Clustering

| Metric | Number of Clusters | AE | CL |
|---|---|---|---|
| **Average Precision** | 5 | 34% | **46%** |
| | 10 | 38% | **40%** |
| | 15 | 37% | **41%** |
| **AUCROC** | 5 | 72% | **74%** |
| | 10 | 67% | **70%** |
| | 15 | 70% | **74%** |
| **Mean IOC** | 5 | 20% | **30%** |
| | 10 | 24% | **30%** |
| | 15 | 24% | **26%** |